Searching for lunar horizon glow with the Lunar Orbiter Laser Altimeter

M. K. Barker[1], E. Mazarico[1], T. P. McClanahan[1], X. Sun[1], G. A. Neumann[1], D. E. Smith[2], M. T. Zuber[2], J. W. Head[3]

[1]Goddard Space Flight Center, 8800 Greenbelt Rd., Greenbelt, MD 20771

[2]Dept. of Earth, Atmospheric and Planetary Sciences, MIT, 77 Massachusetts Ave. Cambridge, MA 02139

[3]Dept. of Earth, Environmental and Planetary Sciences, Brown Univ., Providence, RI 02912

Key Points:

- We searched for forward scattered sunlight from exospheric dust grains, called lunar horizon glow, at altitudes < 20 km
- The sample includes observations throughout ~ 2 years both during and outside of major meteor stream periods
- Assuming a dust grain radius of about 0.1 micron, dust density upper limits are roughly 10 times lower than the density inferred from Apollo 15

Corresponding author: Michael K. Barker, michael.k.barker@nasa.gov

Abstract

We present the results of a 2-year-long systematic campaign to monitor the lunar dust exosphere for enhancements in dust concentration at altitudes < 20 km both during and outside of major meteor stream periods. We utilize the radiometric capabilities of the Lunar Orbiter Laser Altimeter Laser Ranging telescope onboard the Lunar Reconnaissance Orbiter to search for forward-scattered sunlight from exospheric dust grains, called lunar horizon glow (LHG). Specifically, we test the hypothesis that major meteor streams can produce LHG similar to what was measured in Apollo 15 coronal photography. Assuming a one-dimensional exponential vertical dust profile and a dust grain radius $r \sim 0.1$ μm, we derive an upper limit of $\sim 10^{-11}$ g cm^{-2} on the overlying column dust mass density near the terminator during stream periods, a limit roughly 10 times lower than inferred from Apollo 15. Recent studies at altitudes $\sim 1 - 20$ km outside of major meteor streams and at higher altitudes during streams placed limits on the density of similarly-sized grains $\sim 100-1000$ times lower than Apollo 15. Our results show that Apollo 15-like LHG, if real, is also a rare occurrence at altitudes < 20 km during major meteor stream periods. This study is the first to quantitatively constrain the role of meteor streams in producing Apollo 15-like LHG at altitudes < 20 km and small forward-scattering angles, and further narrows the properties of any similar high-altitude LHG and the conditions under which it can occur.

1 Introduction

A thorough understanding of the dust environment of the Moon can enhance many aspects of planetary surface science and exploration (Szalay et al., 2018). As the nearest airless planetary body, the Moon is a cornerstone for understanding how dust grain properties and dust transport processes affect regolith gardening rates, surface spectral properties, and the safety of human and robotic explorers (Bean, 1970; Godwin, 2002; Katzan & Edwards, 1991; Speyerer et al., 2016; Szalay & Horányi, 2016; Costello et al., 2018). One potentially dust-related phenomenon that could reveal information on the dust environment is the so-called lunar horizon glow (LHG), an excess sky brightness observed from Apollo-era orbiters and landers generally in the sunward direction that has been attributed to forward-scattered sunlight from exospheric dust grains near the terminator (Criswell, 1972; Rennilson & Criswell, 1974; McCoy & Criswell, 1974; Severnyi et al., 1975; McCoy, 1976; Zook & McCoy, 1991; Colwell et al., 2007). The inferred

dust densities (~ 0.1 cm^{-3} at the surface) were considered to be too large to be caused by meteoritic impact ejecta (Criswell, 1972; McCoy, 1976). Instead, dust transport models were developed that involved electrostatic levitation of grains with radii $r \sim 5$ μm in the top meter above the surface (Criswell, 1972) and dynamic lofting of grains with $r \sim 0.1$ μm up to $\sim$ 100 km in altitude (Stubbs et al., 2006). Proposed grain mobilization mechanisms have included acceleration by surface electric fields arising from interactions with the local plasma environment and photoemission of electrons from ultraviolet light and X-rays (Criswell, 1972), and the build-up of charge in tiny micro-cavities between grains (Wang et al., 2016).

One of the most thoroughly documented and prominent observations of LHG came from Apollo 15 Command Module coronal photography taken near the dawn terminator by astronaut Alfred M. Worden (McCoy, 1976; Glenar et al., 2011). The LHG extended up to 30 km above the horizon with an excess brightness over the coronal and zodiacal light (CZL) of order 10^{-9} B_{sun} (where B_{sun} is the mean brightness of the solar disk) at an elongation (forward-scattering) angle of 1° to 10^{-10} B_{sun} at an elongation angle of 5°. The large angular dimension of this LHG suggested a grain radius of $r \sim 0.1$ μm (due to the broad forward-scattering lobe of grains of this size), a scale height of ~ 10 km, corresponding to a volume density of ~ 0.01 cm^{-3} at an altitude of 10 km, and a line-of-sight column density at 10 km of order $10^3 - 10^5$cm^{-2}.

However, no excess brightness was seen in other similar photographs taken at the dusk terminator during Apollo 15, 16, and 17. This fact, combined with the observation that the solar wind and UV conditions were quiet during the Apollo 15 measurements, led Glenar et al. (2011) to disfavor the dynamic lofting mechanism as the cause of the Apollo 15 dawn LHG. Instead, they noted that these photographs were taken between the Perseid and Southern Delta Aquariid meteor streams, and hypothesized that meteor stream impact ejecta could initiate a saltation-like cascade process leading to an additional population of lower-velocity ejecta with lower scale height and larger concentration that was responsible for the observed LHG.

More recent searches for LHG with the Clementine Star Trackers (STs) (Glenar et al., 2014) and Lunar Reconnaissance Orbiter (LRO) Lyman Alpha Mapping Project (LAMP) (Feldman et al., 2014) yielded limits on the dust density $\sim 100 - 1000$ times

lower than inferred from Apollo 15. While these LAMP and Clementine studies probed altitudes as low as ~ 1 km, they did not observe during any major meteor streams.

The Lunar Dust Experiment (LDEX), an in-situ dust detector onboard the Lunar Atmosphere and Dust Explorer (LADEE), measured a permanent, although fluctuating, impact ejecta cloud surrounding the Moon (Horányi et al., 2015) with a power-law grain size distribution for $r > 0.3$ μm, the minimum discrete detection threshold of LDEX. The LDEX-based empirical model for the permanent ejecta cloud (Szalay & Horányi, 2016) yields a cumulative concentration at the surface (near the orbital apex) of $r > 0.1$ μm grains that is $\sim 10^5$ times smaller than the Apollo 15 estimate, but this requires extrapolation below the discrete detection limit. Using the LDEX low-energy residual current, Szalay and Horányi (2015) estimated a limit on the density of $r \sim 0.1$ μm grains, assuming a monodisperse (i.e., delta-function) size distribution, at least ~ 100 times lower than the Apollo 15-based density. LDEX operated at altitudes down to $\sim$ 3 km over the whole LADEE mission, but only down to ~ 30 km during major meteor streams, leaving open the question of their role in producing the putative Apollo 15 LHG.

There have also been attempts to observe scattered sunlight from smaller nanodust particles ($r \sim 10$ nm) in the lunar exosphere by looking in the anti-Sun direction to maximize backscattering efficiency. Using UV spectra acquired by the Ultraviolet/Visible Spectrometer (UVS) onboard LADEE during the 2014 Quadrantid meteor shower, Wooden et al. (2016) reported the detection of a UV continuum spectral slope consistent with a population of nanodust particles with $r < 20-30$ nm. They hypothesized that a spatially and temporally variable nanodust exosphere may exist on the Moon that is modulated by meteor showers. In contrast, Grava et al. (2017) found no evidence for a detectable nanodust exosphere in a series of UV spectral observations taken with LAMP during the 2016 Quadrantids. The resulting nanodust line-of-sight column density limits were $\sim 10-100$ times lower than the densities estimated by Wooden et al. (2016). Due to the orbital geometry of these two nanodust studies, they probed altitudes higher than the previous studies (i.e., $\gtrsim 50$ km for UVS and $\gtrsim 150$ km for LAMP).

Finally, we note that atomic emission from the lunar exosphere has been ruled out as a possible source for the Apollo 15 LHG. Although the combined sodium emission line intensities at 589.16 nm and 589.76 nm can approach 10 kR (1 kR $= 10^9/4\pi$ ph s^{-1} cm^{-2} sr^{-1}) in a limb-viewing geometry over the course of a lunation, this corresponds to no more

than a few 10^{-13} B_{sun} for a typical broadband imager with a bandpass of a few hundred nm (Stubbs et al., 2010; Glenar et al., 2014; Colaprete et al., 2016). The total potassium emission at 770.1 nm and 766.7 nm is ~ 5 times weaker than sodium and lies outside the long-wavelength limit of the Kodak film used by Apollo 15 (Colaprete et al., 2016).

These recent developments raise new questions about the temporal and spatial variability of the dust environment and suggest that, if real, Apollo 15-like LHG is more episodic than originally hypothesized. Given the importance of understanding dust transport on airless planetary bodies like the Moon, we present here the results of a two-year-long campaign to search for LHG with the Laser Ranging (LR) system of the Lunar Orbiter Laser Altimeter (LOLA) onboard LRO as part of the LRO Extended Science Mission 3: Cornerstone Mission. Advantages of this LOLA LHG search are that the LR telescope can probe small elongation angles at any time of the year because it is located on the anti-nadir side of the spacecraft; a long time baseline and regular sampling improve the chances of detecting LHG especially if an episodic phenomenon; and we target altitudes < 20 km during major meteor stream periods, a region of parameter space that remains relatively poorly explored. Our goal here is not to measure the permanent ejecta cloud, as this is well below our detection limit, but rather to search for dust clouds with properties broadly similar to those inferred from Apollo 15. We try to be as agnostic as possible regarding the cause of the LHG, e.g., whether it is primary impact ejecta from a more energetic-than-average impact or the result of electrostatic or saltation processes such as those mentioned above, or some combination thereof. With a long-term systematic campaign focusing on the major meteor streams, we can increase the likelihood of seeing any episodic phenomena due to the increased flux during the streams. Contemporaneous observations outside the meteor streams act as a control sample and baseline for comparison.

This paper is organized as follows. In Section 2, we describe the LOLA instrument, observational method, and data sample. In Section 3, we describe the data reduction and modeling of background sources including the CZL. Section 4 describes our approach to modeling lunar dust and Section 5 presents lunar dust upper limits resulting from fitting the data with the lunar dust model and accounting for the CZL. Finally, we summarize the results and make concluding remarks in Section 6.

2 Instrument and Data Description

LOLA is a time-of-flight laser altimeter operating at a wavelength of 1064 nm and a firing rate of 28 Hz (Smith et al., 2010). The instrument has 5 separate silicon avalanche photodiode detectors, or channels, dedicated to each of the 5 laser spots that comprise the LOLA footprint on the lunar surface (Smith et al., 2017).

In Barker et al. (2016), we demonstrated the passive radiometry mode of LOLA for photometric studies of the lunar surface. This instrument mode disables the laser and uses the background noise counts collected by the detectors, which are a function of the number of collected photons over a full rate sampling and integration time of 0.0357 sec. For the photometric observations discussed here, we again use LOLA as a passive radiometer, but instead of using Channels 2−5 at 1064 nm with the LOLA receiver telescope located on the LRO nadir deck, we use Channel 1 with the LR telescope at 532 nm, which is mounted on and co-boresighted with the LRO high-gain antenna (HGA) on the anti-nadir deck. The LOLA-LR telescope was originally used for 1-way ranging between LOLA and Earth-based stations as part of the laser ranging investigation for orbit determination (Zuber et al., 2010; Mao et al., 2017). The LOLA-LR telescope has a 19 mm aperture and 1.75° field-of-view (FOV), and is connected to the LOLA Channel 1 detector assembly via fiber optic cable which feeds the signal through a narrow band filter with central wavelength and band width of 532±0.15 nm. Pre-flight testing of the LR telescope measured an off-axis transmission $< 10^{-6}$ for off-axis angles $> 10°$. The LR telescope can withstand direct solar illumination for periods longer than the 2 hour orbital period of LRO's elliptical polar orbit. By virtue of its location on the opposite side of LRO from the nadir-pointing instruments, the LR telescope can access arbitrarily small solar elongation angles without violating the other instruments' 60° solar keep-out zone. This allows the LOLA-LR system to measure forward-scattered sunlight from exospheric dust both during and outside of major meteor streams throughout the year rather than at very limited time periods of favorable orbital geometry (Feldman et al., 2014).

Table S1 lists the date, location, and other pertinent information for every LOLA-LR LHG observation (also referred to as a scan or limb scan, described in more detail below). The first column gives the scan ID#, a unique, chronological running index number for every scan in the range 1−84. The last column gives the LOLA Reduced Data Record (RDR) in which the scan occurred (format: YYDOYHHMM). All the LOLA data

used here are publicly available from the Planetary Data System Geosciences data node website (`http://pds-geosciences.wustl.edu`).

One of the primary goals of our campaign was to search for LHG during meteor shower periods. We focused on the major Earth-based showers that have the highest flux of micrometeoroids. To maximize the chances of seeing any LHG, we tried to schedule each scan as close as possible to the shower peak times at the Moon, which are $\lesssim 4$ hours from the peak times at the Earth. We were usually successful in obtaining at least two scans during the peak periods despite spacecraft operational constraints (Figure 1). In total, we obtained 84 scans, 76 of which are used in the analysis here. The first 8 were discarded because they had a different threshold setting for Channel 1. The final sample consists of 40 sunrise, 36 sunset, 33 during streams, 43 outside streams, 41 dawn, and 35 dusk scans. Table S1 gives the local solar time and, when applicable, the associated meteor stream.

The 43 scans occurring outside stream periods are designated as the "off-stream" sample. Since we wish to test the hypothesis that the Apollo 15 LHG was related to meteor streams, we more narrowly define an "on-stream" sample including only the 21 scans that occurred in the same hemisphere as the stream radiant (sampling the 2016 Perseids, the 2017 Southern Delta Aquariids, Perseids, and Geminids, and 2018 Quadrantids). The meteoroid flux in the opposite hemisphere as the radiant is zero making it less likely to observe any related LHG there. Each scan's location was calculated not simply as the spacecraft's location (since it could be looking toward or away from the radiant), but as the intensity-weighted mean location of lunar dust grains in the FOV using the lunar dust models in Section 5. A scan was considered to be in the same hemisphere as the radiant if the minimum distance between its location and the radiant in the 200 sec before/after sunrise/sunset was less than 25% of the Moon's circumference. The activity profiles (Figure 1) suggest that the majority of these scans occurred when the stream flux was higher than the sporadic background.

During a typical scan, the HGA is stowed in the spacecraft's $-Z$ (anti-nadir) direction while LRO performs a multi-axis slew so that the HGA and LR telescope are pointed at the limb for several minutes leading up to sunrise. This procedure is essentially reversed for sunset scans (the terms sunrise and sunset refer to the spacecraft's point-of-view from orbit and are distinct from dawn/dusk which refer to an observer on the lu-

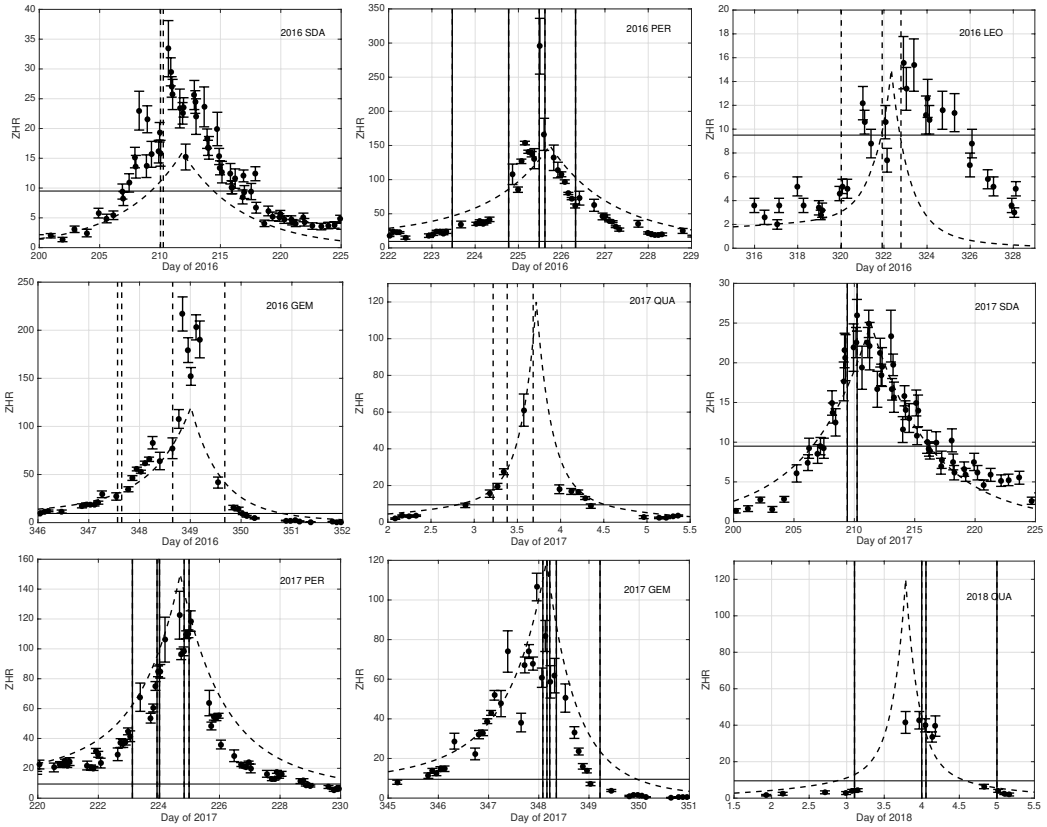

Figure 1. Meteor shower activity profiles based on data (points with error bars) from the International Meteor Organization (IMO) Video Meteor Network (Molau et al., 2018) compared to canonical predictions (dashed curves) from the IMO and Jenniskens (1994), and our scan times (vertical lines). Solid and dashed vertical lines distinguish between scans that occurred in the same or opposite hemisphere as the shower radiant, respectively. The activity profiles have been shifted by the lead/lag times (< 4 hours) due to the position of the Moon relative to the Earth. The sporadic background (horizontal line) has a zenith hourly rate (ZHR) of ∼ 9.5. ZHR is defined as the hourly rate of meteors seen by a standard observer on Earth under optimum conditions when the shower radiant is directly overhead (Jenniskens, 1994). See Table S1 for shower name abbreviations and further details for the whole data sample.

nar surface). Some scans had the HGA stowed in the $\pm Y$ direction (the +Y axis is the anti-Sun side of the spacecraft) to shorten the slewing time. A typical scan probes a range of elongation angles, distances to the terminator, and tangent point altitudes (the height above the lunar surface at the line-of-sight's tangent point to the Moon). LRO is presently in an elliptical polar orbit with periapse of $\sim 30-50$ km above the south pole and apoapse of $\sim 140-160$ km in the north. Thus, the LR FOV, which determines the spatial resolution, is typically $\sim 10-20$ km wide at the horizon and samples a range of tangent point altitudes mostly < 10 km because the lunar limb approximately bisects the FOV. Because of the polar orbit, these observations tend to occur at high latitude, but as the beta angle (the angle between the Sun and the orbital angular momentum vector) shifts throughout the year, there are periods when eclipse occurs closer to the equator. Due to the high-altitude observing geometry and large FOV of the LR telescope, altitudes < 1 km are usually in shadow or contribute little to the measured signal. Thus, any LHG occurring entirely within ~ 1 km of the surface is unconstrained by these measurements.

All of the measurements used in our analysis take place when the spacecraft is in shadow. The Sun is within or just outside the FOV at sunrise or sunset, saturating the detector and marking the ending/beginning of each sunrise/sunset scan time series. Many of the scans occur on the lunar near side where the Earth could be a potential illumination source. Therefore, in our analysis of each scan, we track the Earth elongation relative to the LR telescope and the LOLA receiver telescope because any light entering either telescope (at 532-nm or 1064-nm, respectively) will contribute to the measured signal in Channel 1. Earth radiance directly into either telescope is avoided by excluding Earth elongation angles $< 2°$. Earthshine reflected off the lunar surface (see Section 3.4) is estimated to generally be well within the measurement noise.

Figure 2 depicts the observation and illumination geometry for the last two minutes of scan #9 on 2016 day-of-year (DOY) 099. LRO (magenta points) was in shadow moving south and oriented with the LR telescope pointing toward the Sun in the direction of the cyan lines. The shadow boundary (yellow points) and surface locations (green points) within the FOV are calculated as described in Section 3.

Figure 3 summarizes relevant information for this scan as a function of seconds of orbit defined such that $t = 0$ is the ascending node (near the equator). It shows the angular separation of the LR FOV, the Sun, and the topography relative to the refer-

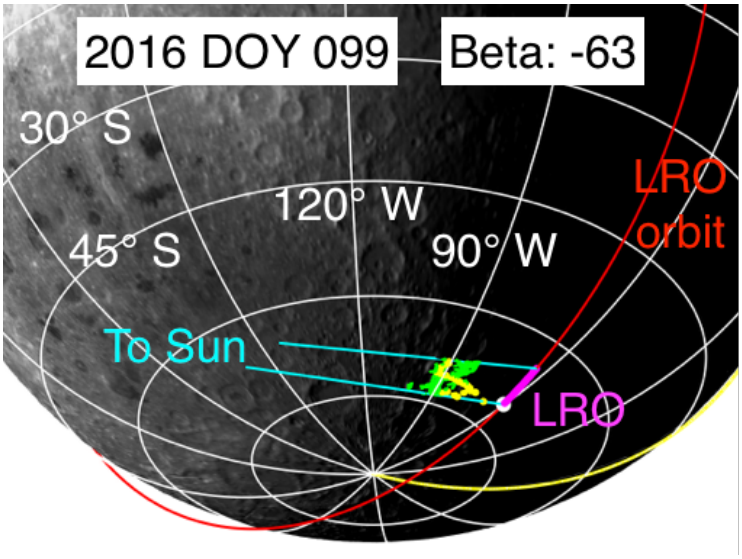

Figure 2. Observation and illumination geometries for the last two minutes of scan #9. LRO (magenta points) was in shadow moving south and oriented with the LR telescope pointing towards the Sun. The two cyan lines are 1000-km-long LR boresight vectors at two minutes prior to sunrise and at sunrise (white dot). Surface locations within the LR FOV at these times are green points. Yellow points represent the shadow boundary along the LR boresight. The central meridian is in yellow.

ence sphere (1737.4-km radius) sampled at the tangent point of the LR FOV's central boresight vector. Because this figure only samples one point at one distance, it gives only an approximate sense of the topographic scale within the FOV. A more detailed ray-tracing calculation covering the whole FOV is presented in Section 3. The FOV and Sun can both be close to the limb while still being far apart, so this figure also shows the elongation angle between the Sun and FOV as the magenta line. The red line is the measured signal in counts / sec, which saturates at sunrise.

Figure 4 shows a close-up of the data for this particular scan. We average the data into 4-sec bins with 112 points per bin to increase the signal-to-noise ratio. The steady-state equivalent brightness prior to $\sim$ 4900 sec results from the detector dark current, which varies slowly with detector temperature, causing a slight decline in signal. The rise in counts starting at $\sim$ 4900 sec is due to the CZL, which we use as a reference source to calibrate the LOLA-LR system's counts/sec to an absolute radiance scale (B_{sun}). Section 3.1 and Section 3.2 provide additional details on how the dark current and CZL are

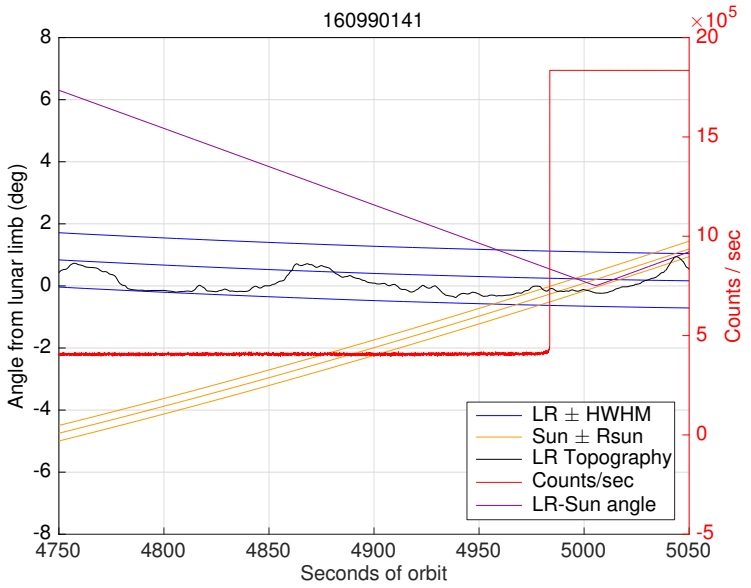

Figure 3. Angular separation of the Sun (orange lines) and LR FOV (blue lines) from the reference sphere horizon for scan #9. The black line is the height of the topography relative to the reference sphere sampled at the tangent point of the LR FOV. The magenta line shows the elongation angle between the Sun and LR central boresight. The signal measured by the LR telescope is depicted with the red line and right-hand y-axis.

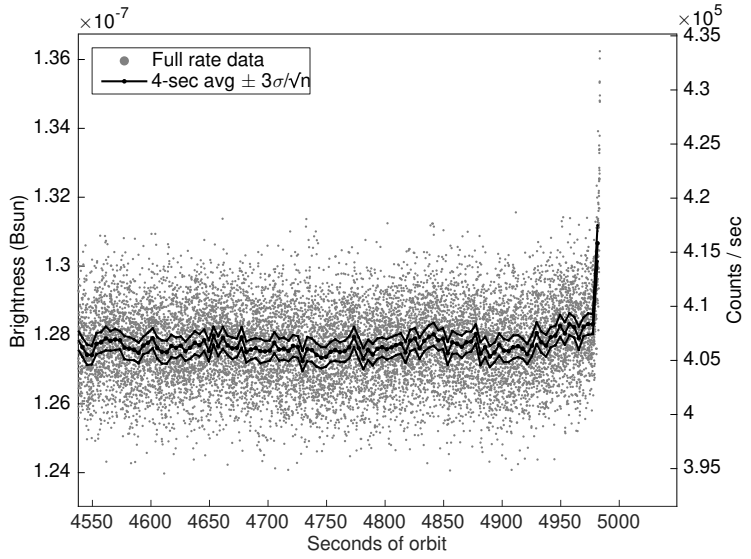

Figure 4. Full rate data (gray points) for scan #9 and the 4-sec average ±3 times the standard error of the mean (black points and lines). The detector dark current causes the slight decline in signal prior to ∼ 4900 sec at which time the signal begins to rise due to the CZL.

modeled and the radiance calibration. The vast majority of the data we use for all scans are more than 4 times less than the saturation level of 1.8×10^6 counts/sec, or 5.7×10^{-7} B_{sun} at 532 nm ($1\ B_{sun} = 2.84 \times 10^7$ W/m^2/μm/sr at this wavelength). Since the detector response is linear up to at least half the saturation level (see Section 3.4), the data are within the linear response regime of the detector.

3 Data Reduction and Background Sources

The time-variable signal output by LOLA during a scan consists of a dark current due to thermal electrons in the detector electronics, and several possible sources of light entering the telescopes: the CZL (for those scans that reach low enough elongation), surface-scattered light from the Earth or Sun, and the hypothetical lunar dust component (the signal of interest). Because the LR FOV is so large, we must sub-sample it in post-processing with many boresights, and perform 3-D ray tracing on each one to simulate incoming radiation. In this section, we describe in more detail the modeling approach for each of these components.

3.1 Dark-current

Thermal electrons within the detector electronics give rise to a non-zero output signal even in darkness. This dark current depends primarily on detector gain and temperature, and, to a lesser extent, on time due to a long-term drift. All of the scans used the same threshold except for the first 8 which are discarded in the analysis. The detector temperature typically varies in a sinusoidal fashion throughout an orbit with an amplitude that decreases with increasing beta angle (Figure S1). The detector temperature is recorded as part of the LOLA housekeeping telemetry and available from the PDS in the Experimental Data Record (EDR) for each orbit. Approximation with piecewise cubic splines, separated by 7 nodes per orbit, smoothes discrete steps in temperature due to the EDR temperature record's limited precision. Over the limited time period of interest for each scan, the temperature controls the general decrease in signal with time (Figure 5). Thus, we fit the dark current for each scan individually as a linear function of time. When combined with a CZL model (Section 3.2), this yields the null-hypothesis models (no lunar dust) plotted as colored points in Fig. 5. The standard deviation of the null hypothesis model residuals is $\sim 2-3\times10^{-10} B_{sun}$ and sets the single-point detection limit for a signal-to-noise ratio of one. We chose 900 sec as the maximum time range

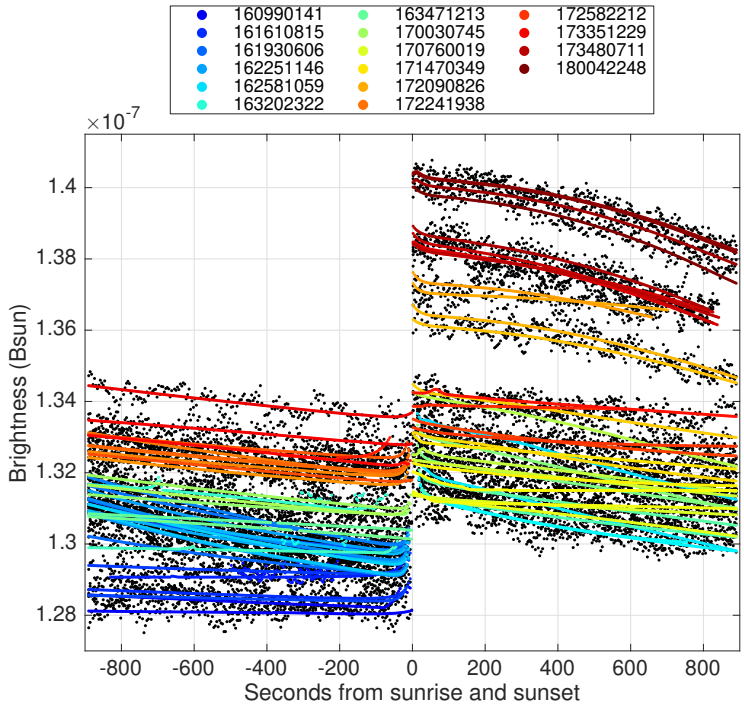

Figure 5. The observed signal during each scan (black points) averaged over 4 sec intervals. Best-fit null hypothesis (dark current plus CZL, no lunar dust) models are overplotted as colored points on a continuous color scale in chronological order (only a subset are listed in the legend). The detector temperature controls the general decrease in signal with time. The CZL is usually only apparent within ~ 30 sec of sunrise/sunset.

to analyze for each scan although the results are not especially sensitive to this value; 600 or 1200 sec did not change the results significantly. This was a compromise between the desire to have enough time to measure the dark current and to treat all the scans as consistently as possible (about 10% of the scans last for < 800 sec).

3.2 CZL model

The CZL model is based on images acquired by the Solar and Heliospheric Observatory (SOHO) Large Angle and Spectrometric Coronagraph Experiment (LASCO) C2 and C3 instruments (Morrill et al., 2006). The C2 and C3 instruments have pixel scales of 12 and 58 arcsec, FOVs that extend to elongation $\sim 1.8°$ and $\sim 8°$, and separate occulters that block out the region inside 0.7° and 1°, respectively. The C2 images were

acquired with the orange filter ($\sim 540-640$ nm) and the C3 images were acquired with the clear filter ($\sim 400-900$ nm).

LASCO images taken contemporaneously with our scans were not yet available from the Naval Research Laboratory LASCO website (`https://lasco-www.nrl.navy.mil`) at the time of this analysis. Therefore, we constructed a single master composite CZL image to apply to all scans when simulating the CZL background. This master image was obtained by combining 24 equally-spaced C2/C3 image pairs from 2005, when the Sun was at a similar point in its 11-year activity cycle. In a process similar to that used by the LASCO processing pipeline, we take the minimum pixel value out of all images, which removes most of the transient K-corona structures and leaves the static F-corona and long-lived K-corona (Hayes et al., 2001; Glenar et al., 2014). The images are calibrated to B_{sun} units, but due to the different filters, we had to multiply each C2 image by a scale factor of $1.2-1.3$ to align the pixel brightness values with those in the corresponding C3 image. This factor was determined by sampling the C3 image at the C2 pixel locations in the overlap area between the two instruments ($\sim 1.4-2.0°$). The mean ratio, C3/C2, of pixel values for each pair ranged from $\sim 1.2-1.3$ with a standard deviation of $0.05-0.10$. Then, the region in the C3 image covering elongation $<$ $1.4°$ was replaced with the corresponding region in the C2 image using 2-dimensional bilinear interpolation onto the same pixel grid. Figure 6 shows the resulting master CZL image.

For seven scans, a portion of the unobscured FOV reaches elongation angles inside the C2 occulter radius, so it proved useful to fill that region with a 2-dimensional model (Giese et al., 1986; Hahn et al., 2002) fit to the C2 image outside the occulter and extrapolated inward. However, given the uncertainties inherent in this procedure, any points with a contribution from that region (about $15-85$ points in these scans) are excluded from all model fitting.

The master composite image filtered out the time-variable K-corona leading, on average, to an underestimate of the true CZL signal measured in our limb scans despite the smoothing effect of the large FOV. To investigate this further, we obtained C2/C3 images taken within the same hour as 12 scans in 2016 from the LASCO team (K. Battams, private communication) and combined them in the manner described above. These additional near-coincident LASCO images were not merged into the master, but are used

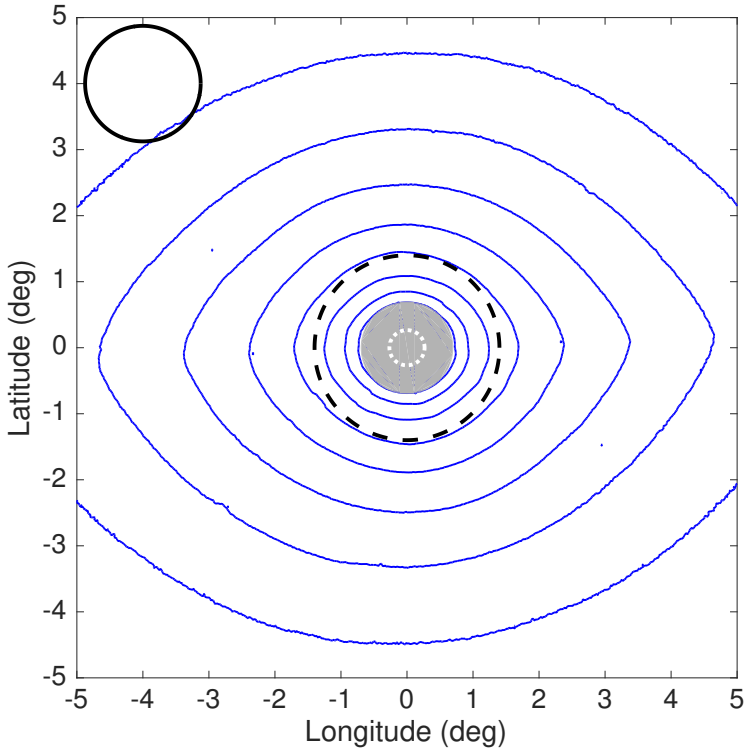

Figure 6. Master composite image of the CZL constructed from LASCO C2 and C3 images inside and outside the dashed black line, respectively. Contours start at 4 × 10^{-11} B_{sun} (outermost) and increase by factors of 2. The innermost dashed white circle is the Sun's disk, the gray shaded circle is the C2 occulter. The black circle in the upper left corner is the LR FOV, for reference.

to quantify any excess light from the transitory K-corona, and to derive the radiometric calibration for the LOLA-LR system (see below). We convolved the composite images with a circular top-hat filter with an area of one-half that of the LR FOV to approximate a 50% occultation by the Moon, as is roughly the case in many scans. Comparison between the smoothed master and individual images (Figure 7) shows that the time-variable K-corona (including streamers) could cause enhancements of $\sim (0.5{-}5)\times 10^{-9}$ B_{sun} at 0.7° and $\sim (0.1{-}1)\times 10^{-9}$ B_{sun} at 1.0°. In terms of fractional enhancement over the smoothed master, the K-corona ranges from ~ 0.1 to 0.6 at 0.7° and $\sim$ 0.05 to 0.5 at 1.0°. The mean and standard deviation of enhancements decreases from $(2.2\pm0.5)\times10^{-9}$ B_{sun} at 0.7° to $(1.1\pm0.6)\times10^{-11}$ B_{sun} at 4° corresponding to fractional enhancements of ~ 0.25 to 0.15. The declining solar activity through 2016 causes the temporal trend in the residuals suggesting that the 2017 scans may have smaller resid-

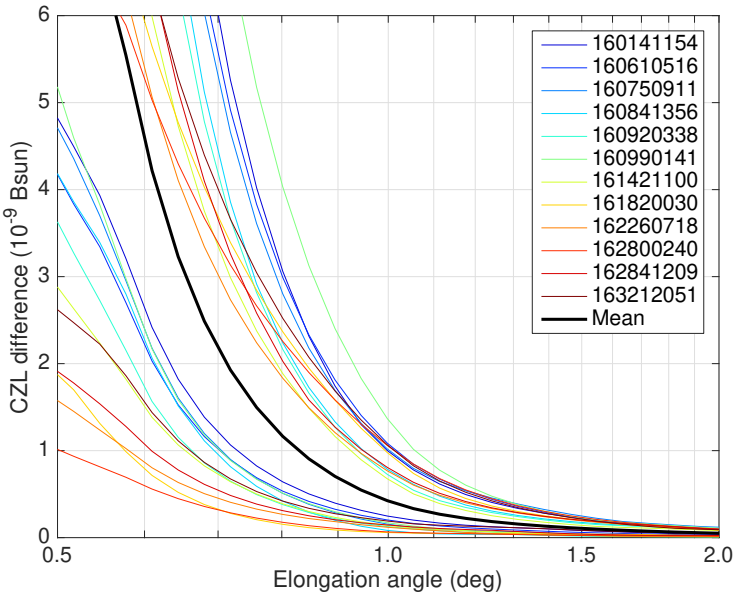

Figure 7. Difference between LASCO images and the master composite CZL image versus elongation angle on a log scale. The LASCO images were taken within the same hour as the LOLA RDR times listed in the legend. The upper and lower sets of lines show the maximum and minimum residuals over all position angles, respectively, after smoothing with a top-hat filter 1.2° wide. The mean residual (black line) is $(2.2\pm0.5)\times10^{-9}$ B_{sun} at 0.7° and $(1.1\pm0.6)\times10^{-11}$ B_{sun} at 4° corresponding to fractional enhancements of ~ 0.25 and 0.15, respectively.

uals on average. In Section 5, we discuss the potential impact of excess brightness from the K-corona on the lunar dust search, which can cause a small overestimate of the lunar dust density, but does not significantly affect the overall distribution of retrieved densities or our conclusions.

The CZL signal that the LOLA-LR system measures in a particular scan depends on the elongation angle and sky visibility within the FOV, namely, the fraction of the FOV unobscured by the Moon. To estimate the sky visibility and resulting CZL model, we sub-sample the FOV with 500 boresights at 4-sec intervals and determine whether each boresight intersects the 64 pixel-per-degree (ppd) LOLA lunar shape model using the 3-D ray-tracing illumination software package, IllumNG (Mazarico et al., 2018, 2011). A resolution of 64 ppd corresponds to approximately 470 m at the equator, 330 m at 45° latitude, and 80 m at 80° latitude. If a boresight intersects the lunar surface, it is assigned a value of zero, otherwise it gets the CZL value it would measure on the corre-

sponding intersection point with the sky. The total CZL model signal is then the average of all boresights. Finally, we multiply this value by a small correction factor of 0.94 to account for the different spectral response of the LASCO clear filter and LOLA-LR system,

$$\frac{(B/B_{sun})_{LR}}{(B/B_{sun})_{clear}} = \frac{\int F_{\odot} C(\lambda) R_{LR}(\lambda) d\lambda}{\int F_{\odot}(\lambda) R_{LR}(\lambda) d\lambda} \frac{\int F_{\odot}(\lambda) R_{clear}(\lambda) d\lambda}{\int F_{\odot} C(\lambda) R_{clear}(\lambda) d\lambda} \quad (1)$$

where R_{clear} is the response curve of the LASCO clear filter (Morrill et al., 2006), R_{LR} is the response curve of the LOLA-LR system, which we treat as a delta-function centered on 532-nm, and $C(\lambda)$ is the color of the zodiacal light (Leinert et al., 1998).

The resulting CZL model and visibility for scan #9 are shown in Figure 8 together with the dark-subtracted data. We use this scan to derive the radiometric calibration to transform counts/sec to B_{sun} because it is one of the few for which we have a relatively robust CZL detection and a near-coincident LASCO image to act as the reference. Here, we use the near-coincident LASCO image instead of the master to derive the CZL model because we need a photometric standard giving the total radiance entering the LR telescope at the time of the scan. The best-fit scale factor that brings the measured LOLA-LR signal into agreement with the near-coincident CZL model is 3.16×10^{-13} B_{sun}/(counts/sec) and we apply that same scale factor to all the other scans. Three points at 4953−4961 sec and the last point at 4981 sec are excluded from the fit because they have at least one unobscured boresight within the C2 occulter, where the CZL model is less reliable. We estimate an uncertainty of 40% by perturbing the scale factor away from its best-fit value until the data-model residuals are commensurate with the dark noise standard deviation of $\sim$ 570 counts/sec or $\sim 2 \times 10^{-10}$ B_{sun}. There is no correction made for long-term drift in this scale factor, but we expect it to be similar to the other detectors, or $\leq 5\%$ per year (Barker et al., 2016).

New topography continuously moves through the FOV changing the sky visibility uniquely for every scan. This is more clearly seen in the data at higher beta angle, when the Sun barely grazes below the horizon for several orbits. During these orbits, it is possible to stare at a fixed elongation angle for several minutes from sunset to sunrise. Figure 9 shows one such grazing "double-scan" (scan #11) when the central boresight elongation angle was fixed at $\sim 0.7°$. Fluctuations in the signal are correlated with the sky visibility indicating that the signal is dominated by a source in the sky. The CZL model compares well with the data especially during the periods 6321 − 6409 sec and 6457 −

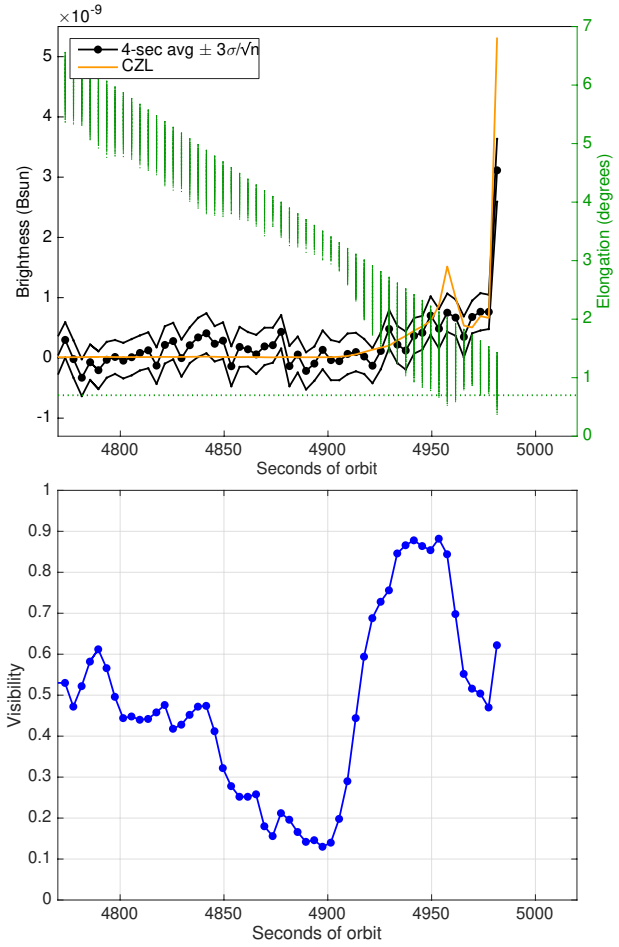

Figure 8. Top panel: Dark-subtracted signal (black points) for scan #9 compared to the CZL model (orange line) using near-coincident LASCO images. The upper and lower black lines denote ±3 times the standard error of the mean in each bin ($3\sigma/\sqrt{n}$). The band of green points and right-hand y-axis show the elongation angle of unobscured boresights. Points with any unobscured boresight within the C2 occulter radius (0.7°, horizontal dotted line) are excluded in the model fitting of all scans. Bottom panel: Visibility for this scan (the fraction of the FOV unobscured by the Moon).

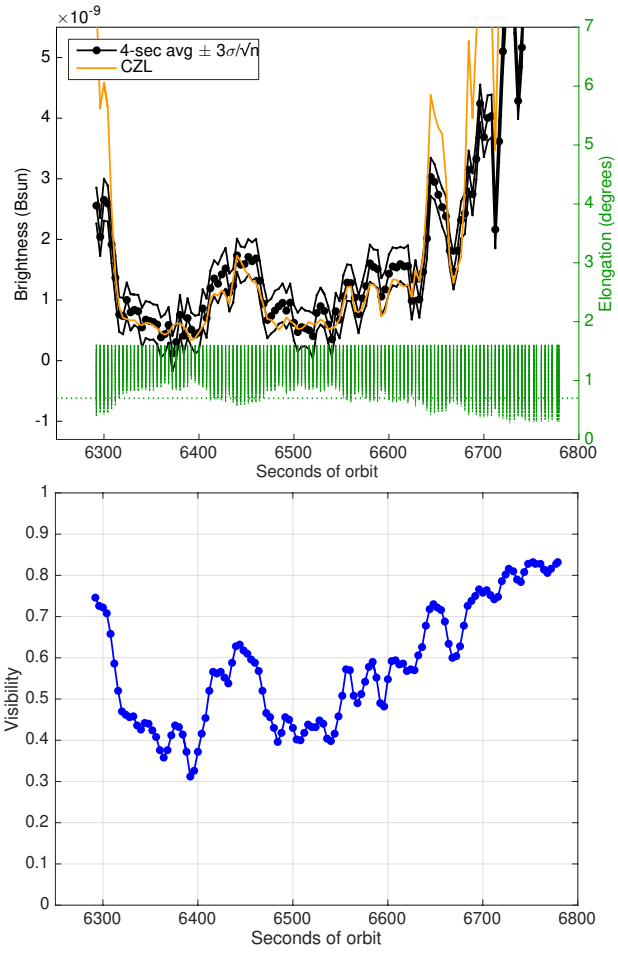

Figure 9. Same as Fig. 8 but for a grazing double-scan fixed at a central boresight elongation $\sim 0.7^\circ$ from sunset to sunrise (scan #11).

6552 sec when no boresight was within the C2 occulter radius. We note that the radiometric calibration scale factor derived from this scan is within a few percent of the adopted value despite a more uncertain dark current due to a lack of dark time for such grazing double-scans.

3.3 Surface-scattered sunlight

Another potential signal source which we considered was surface-scattered sunlight. In our observing geometry, the Sun is below the horizon from LRO's perspective, but the surface region within the FOV is hundreds of km closer to the terminator where elevated terrain may be high enough to be illuminated. However, conditions must be finely-

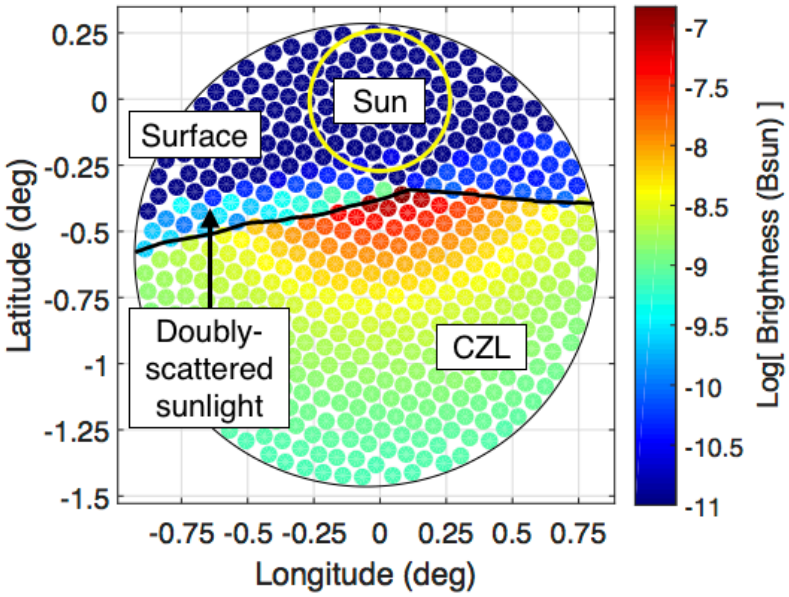

Figure 10. Simulated image of the LR telescope FOV with CZL and surface-scattered sunlight. The thick black line is the lunar limb. The axes are Geocentric Solar Ecliptic coordinates. The figure shows a snapshot when LRO was in the southern hemisphere, which causes the orientation of the sky and surface to appear upside-down relative to a typical horizon scene. For plotting purposes, the boresights, which are zero-dimensional points, are represented as circles with finite width to more clearly show their colors. Hence, some of the circles extend slightly past the limb.

tuned for a surface facet to face both the Sun and LRO at the low elongation angles studied here. We performed 3-D ray-tracing scattering simulations for the 80 sec from sunset/sunrise in seven of our scans using IllumNG, which accounts for obscurations by lunar terrain between the Sun and Moon and the Moon and LRO. There were no instances of this singly-scattered sunlight within the FOV. We did find, however, a small contribution from doubly-scattered radiation, sunlight hitting the surface twice. Such double bounces occur on distant, elevated terrain or high peaks at moderate phase angles $< 90°$ where the first bounce is back toward the Sun and the second is toward LRO. The magnitude of this doubly-scattered light was typically less than a few $\times 10^{-11} B_{sun}$ (Figure 10), and often orders of magnitude lower. The magnitude is heavily dependent on the particular topography and observation/illumination geometry, but we think that it is reasonable to ignore any such signal since it is much less than other sources.

3.4 Earthshine

Another potential source of radiation is earthshine, sunlight reflected off the Earth and then the Moon into either telescope. We used IllumNG to estimate the contribution of earthshine to each scan through both the LR telescope (at 532-nm) and the LOLA receiver telescope (at 1064-nm). The signal measured by Channel 1 is a superposition of the radiance entering both telescopes. The Earth is modeled with a spherical (Bond) albedo of 0.3 (Stephens et al., 2015) and its surface is divided into 671 Lambertian facets of roughly equal area. The Earth radiance predicted by IllumNG was validated against the model of Glenar et al. (2019) and found to generally agree to within 30%. The lunar reflectance is modeled with the mean highlands photometric function at 566-nm (Sato et al., 2014) and 1064-nm (Barker et al., 2016). As before, partial or full obscuration by the lunar terrain is accounted for in the ray tracing. To convert the model 1064-nm earthshine into counts/sec we obtained a preliminary near-IR radiance calibration for Channel 1 (Supplementary Information). The sum of the counts/sec at both 1064-nm and 532-nm was then scaled into an effective 532-nm radiance using the same calibration factor as for the data.

Earthshine would only be visible in the 60% of scans occurring on the lunar near side. Due to the predominantly grazing geometries encountered during the scans, about half of the near side scans have earthshine levels $< 1 \times 10^{-11} B_{sun}$ while the rest have levels $\lesssim 10^{-10} B_{sun}$. Given that this is less than the typical dark-current noise of the 4-sec averaged data, we make no correction for earthshine in the analysis that follows.

3.5 Averaged measurements

Previous sub-sections described the data reduction and modeling strategy for the relevant background sources. With these in hand, we can begin to look for trends in the dataset as a whole. As a first step, Figure 11 shows the null-hypothesis dark-subtracted measurements averaged and plotted against the mean elongation angle of unobscured boresights. Here the data have been normalized to a visibility of unity by dividing each point by its unique visibility calculated as described above. Points with any unobscured boresight inside the C2 occulter radius (0.7°), which are excluded from the model fits here and in the following sections, are colored orange whereas points with all unobscured boresights outside this radius are colored gray. The orange and gray points overlap in

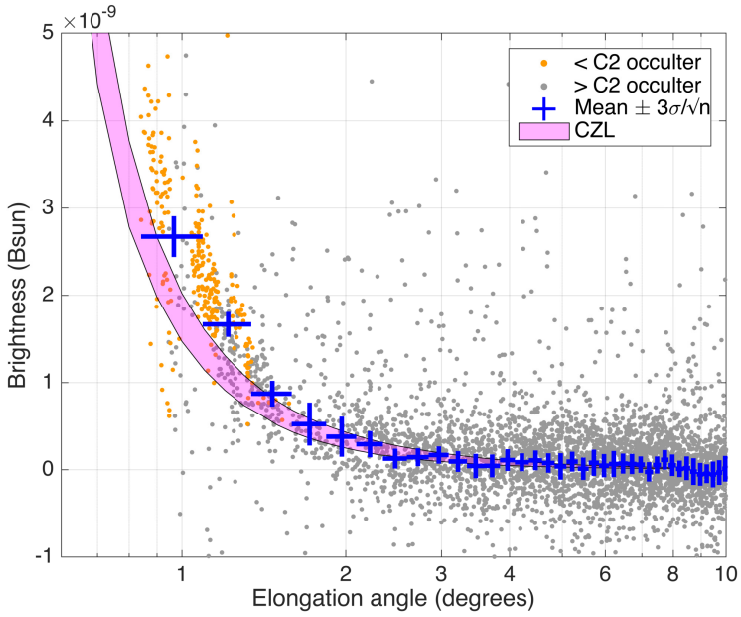

Figure 11. All measurements versus the mean elongation angle of unobscured boresights on a log scale. Points with any unobscured boresight inside the C2 occulter radius (0.7°) are colored orange whereas points with all unobscured boresights outside this radius are colored gray. Blue points with error bars show the mean of all measurements. Vertical error bars are 3 times the standard error of the mean and horizontal error bars are the bin widths. The pink shaded region is the range of master CZL values over all position angles. The measurements are dominated by the CZL at elongation $\lesssim 3°$.

elongation range due to the variable lunar topography in the FOV. The averaged measurements show a consistent detection of the CZL at elongation $\lesssim 3°$ with an excess brightness of $\sim 0.2-0.8\times10^{-9}$ B_{sun} over the master CZL image inside $\sim 1.5°$. This excess is due almost entirely to points with any unobscured boresight inside the C2 occulter radius and is within the range of K-corona enhancements in Figure 7. Other points lying above the CZL may be due to a lunar dust component, but inverting the data in this way increases the scatter. Instead, in the following sections, we perform forward-modeling with a physically-motivated lunar dust model to predict the observed brightness.

4 Lunar dust model

To model the hypothetical lunar dust component, we adopt a 1-dimensional dust model wherein the dust grain number density decreases exponentially with altitude with

exponential scale height, h, from a surface-level density, n_0 (Glenar et al., 2014; Feldman et al., 2014). As with the CZL model, we subsample the FOV with 500 boresights and integrate the dust density along the illuminated portion of each, obtaining the dust column density along the line-of-sight. The column density is then multiplied by the grain radiance to yield the predicted brightness of the model. We compute the grain radiance, G, as a function of wavelength λ, elongation angle ϵ, and grain size distribution, $n_r(r_p, w)$, normalized to unity with peak radius r_p and width parameter w, integrating over the size distribution,

$$G(\lambda, \epsilon, r_p, w) = F_\odot(\lambda) \int \pi r^2 Q_{sc}(\lambda, r) P(\lambda, r, \epsilon) n_r(r_p, w) dr, \tag{2}$$

where $F_\odot(\lambda)$ is the solar spectrum, πr^2 is the grain cross section, $Q_{sc}(\lambda, r)$ is the grain scattering efficiency, and $P(\lambda, r, \epsilon)$ is the normalized, polarization-averaged phase function for single scattering. For the solar spectrum, we use the Laboratory for Atmospheric and Space Physics on-line interactive database of solar irradiance spectra measured by the Solar Radiation and Climate Experiment (SORCE; `http://lasp.colorado.edu/lsird/`). To calculate the scattering efficiency and phase function, we use Mie scattering theory (van de Hulst, 1957) and adopt a dust grain real refractive index $n = 1.60$, within the range found for Apollo samples $n = 1.56 - 1.67$ (King et al., 1971; Kim et al., 1971), and an imaginary refractive index $k = 0.0006$, within the range $0.0005{-}0.001$ derived from models at visible wavelengths (Egan & Hilgeman, 1973; Shkuratov et al., 1999).

Converting the grain radiance, B_{gr}, to units of B_{sun} in general requires integrating over the observer's filter response curve $R(\lambda)$,

$$\frac{B_{gr}(\epsilon, r_p, w)}{B_{sun}} = \frac{\Omega_\odot \int G(\lambda, \epsilon, r_p, w) R(\lambda) d\lambda}{\int F_\odot(\lambda) R(\lambda) d\lambda} \tag{3}$$

where $\Omega_\odot$ is the surface area of the solar disk in steradians. As before, we treat the LOLA-LR system bandpass as a delta-function centered on 532-nm.

In their re-analysis of the Apollo 15 LHG measurements, Glenar et al. (2011) adopted a monodisperse grain size distribution centered at $r = 0.1$ μm. To approximate naturally occurring grain size distributions, later studies searching for LHG adopted a log-normal distribution with a peak at $r_p = 0.1$ μm and a width such that 99% of grains have $r < 2r_p$ (Feldman et al., 2014; Glenar et al., 2014). In either case, the grain radiance is approximately constant for the small elongation angles relevant here (Figure 12).

This leads to an easy conversion between the grain radiance obtained with the monodisperse and with the log-normal distributions. To facilitate comparison of our results with the LHG studies of those authors, we adopt the log-normal distribution grain brightness at 532-nm, 1.20×10^{-14} B_{sun}/(grains cm^{-2}). Using this conversion factor, the standard deviation of the dark current model residuals (Section 3.1) corresponds to a line-of-sight column density of $\sim 1.5 - 2.5 \times 10^4$ cm^{-2}.

Subsequent to those studies, the LADEE-LDEX instrument measured a power-law size distribution in the permanent ejecta cloud for $r \geq 0.3$ μm, the minimum radius directly detectable by LDEX (Horányi et al., 2015). The LDEX size distribution yields a grain radiance that decreases strongly with elongation angle and an overall higher grain radiance (Figure 12). While it is beyond the scope of the present work to re-derive dust density limits of the previous LHG studies, we note that adopting the LDEX grain size distribution would likely lead to qualitatively lower inferred densities than the monodisperse or log-normal distributions because fewer grains would be needed to match a given observed brightness.

Similar calculations for the Kodak film used in the Apollo 15 measurements yield a scaling factor of ~ 3 to convert the Kodak monodisperse grain radiance to the equivalent log-normal radiance. We use this factor to scale the Apollo 15-based dust density of Glenar et al. (2011) from $n_0 = 0.03$ to 0.01 cm^{-3}. We adopt a scale height of $h = 8.5$ km, within the range $\sim 3-12$ km inferred from the Apollo 15 measurements (Glenar et al., 2011). Figure 13 shows the LHG signal computed as described above for this fiducial Apollo 15 model for a subset of scans. The model tends to rise above the dark current residuals at $\sim 100 - 300$ sec with a maximum of $\sim 1.8 \times 10^{-9} B_{sun}$ or a line-of-sight column density of $\sim 1.5 \times 10^5$ cm^{-2}.

5 Results

We model the data as the sum of the dark current, CZL, and the lunar dust model computed as described above. We model the full time series of each scan during which the hypothetical LHG signal changes due to the evolving geometry and visibility. This task requires disentangling all 3 components by exploiting their different behaviors with time. Fitting them simultaneously allows for correlations between the components. Although the CZL and LHG signals behave qualitatively similarly, the CZL is not a free

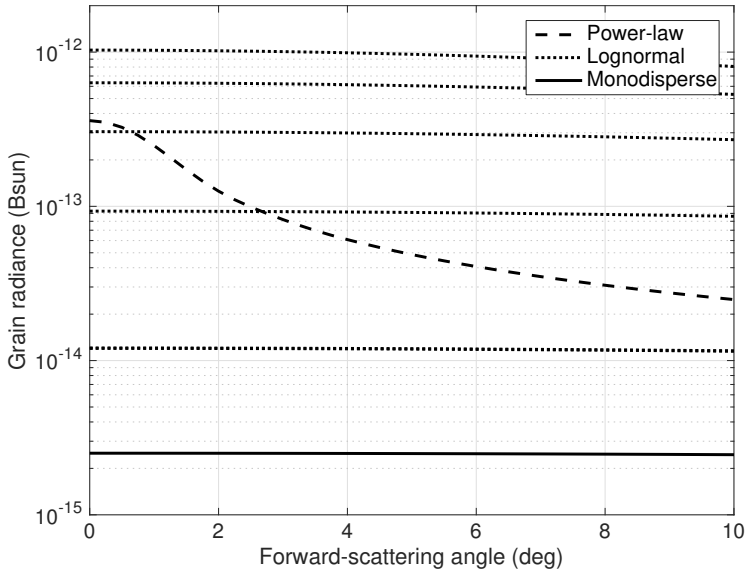

Figure 12. Single-grain radiance at 532-nm as a function of forward-scattering (elongation) angle for different dust grain size distributions: mono-disperse with $r = 0.1$ μm (solid line), log-normal with $r_p = 0.1, 0.15, 0.2, 0.25, 0.3$ μm (dotted lines, bottom to top, used in this study), and LADEE-LDEX size power law with coefficient 0.91 and minimum radius $r_{min} = 0.05$ μm (dashed line). Increasing r_{min} to 0.3 μm shifts the dashed line up by a factor of $\sim$ 100 while keeping the overall shape the same to within $\pm$15%.

parameter, but rather a lower limit, which means that the resulting LHG density is an upper limit. Because our spatial resolution at the limb is typically around 10 km, we can only place upper limits on the vertical overlying column density, $n_0 h$. Working in terms of the overlying column density has the advantage of being less dependent on observation/illumination geometry and spatial resolution than the line-of-sight column density. The only free parameters are the slope and zero-point of the dark current relation and the product $n_0 h$, which we constrain to be ≥ 0. Changing $n_0 h$ from the fiducial value of 8500 cm^{-2} has the effect of re-scaling the curves in Figure 13.

The resulting best-fit models for a few example scans in the off-stream and on-stream samples are shown in Figure 14 and Figure 15, respectively. The scans are offset vertically from bottom to top in order of increasing $n_0 h$. The best-fit model (red line) is usually smaller than the Apollo 15 fiducial model (black line, $n_0 h = 8500$ cm^{-2}). Changing the scale height from its nominal value of 8.5 km to 3 km or 12 km generally has a small effect on the model profile that can be compensated by scaling n_0 (Figure S3). The

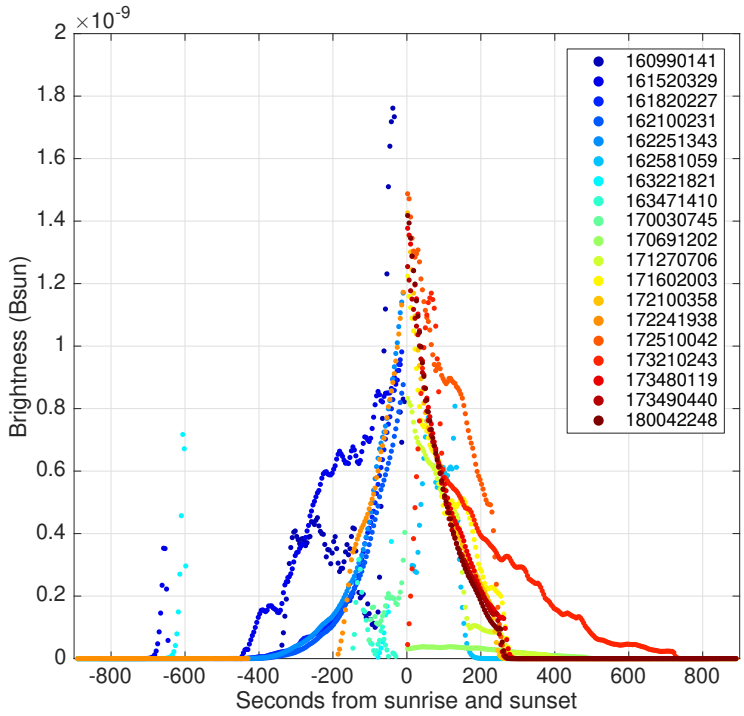

Figure 13. The fiducial Apollo 15 model ($n_0 = 0.01$ cm^{-3}, h $= 8.5$ km) for a subset of scans colored by chronological order.

best-fit value of $n_0 h$ increases or decreases by roughly 20−30% for $h = 3$ km or 12 km, respectively.

Inspection of each scan's time series shows that the dark noise can be as large as, or larger than, the fiducial Apollo 15 model, but the large sample size allows us to overcome the limited ability of any single scan alone to constrain the LHG dust density. The median $n_0 h$ for the whole sample is 416 cm^{-2} and the 75th percentile is 2163 cm^{-2}. The on-stream sample has a median $n_0 h = 781$ cm^{-2} while the off-stream sample has a median $n_0 h = 214$ cm^{-2}. This difference is suggestive, but not statistically significant, and is well within the spread of best-fit $n_0 h$ values: the 75th percentiles for the on-stream and off-stream samples are 1872 cm^{-2} and 2967 cm^{-2}, respectively. Dawn/dusk, sunrise/sunset, and near/far side samples show similar levels of consistency.

Roughly 60% of the best-fit models have $n_0 h > 10$ cm^{-2}, with a median value of 1849 cm^{-2}, and the remaining 40% have $n_0 h < 10^{-8}$ cm^{-2}. We attribute this apparent bimodality to the fact that $n_0 h$ was constrained to be ≥ 0. Repeating the fits with $n_0 h$ unconstrained (where a negative value reflects the curves in Figure 13 about the x-

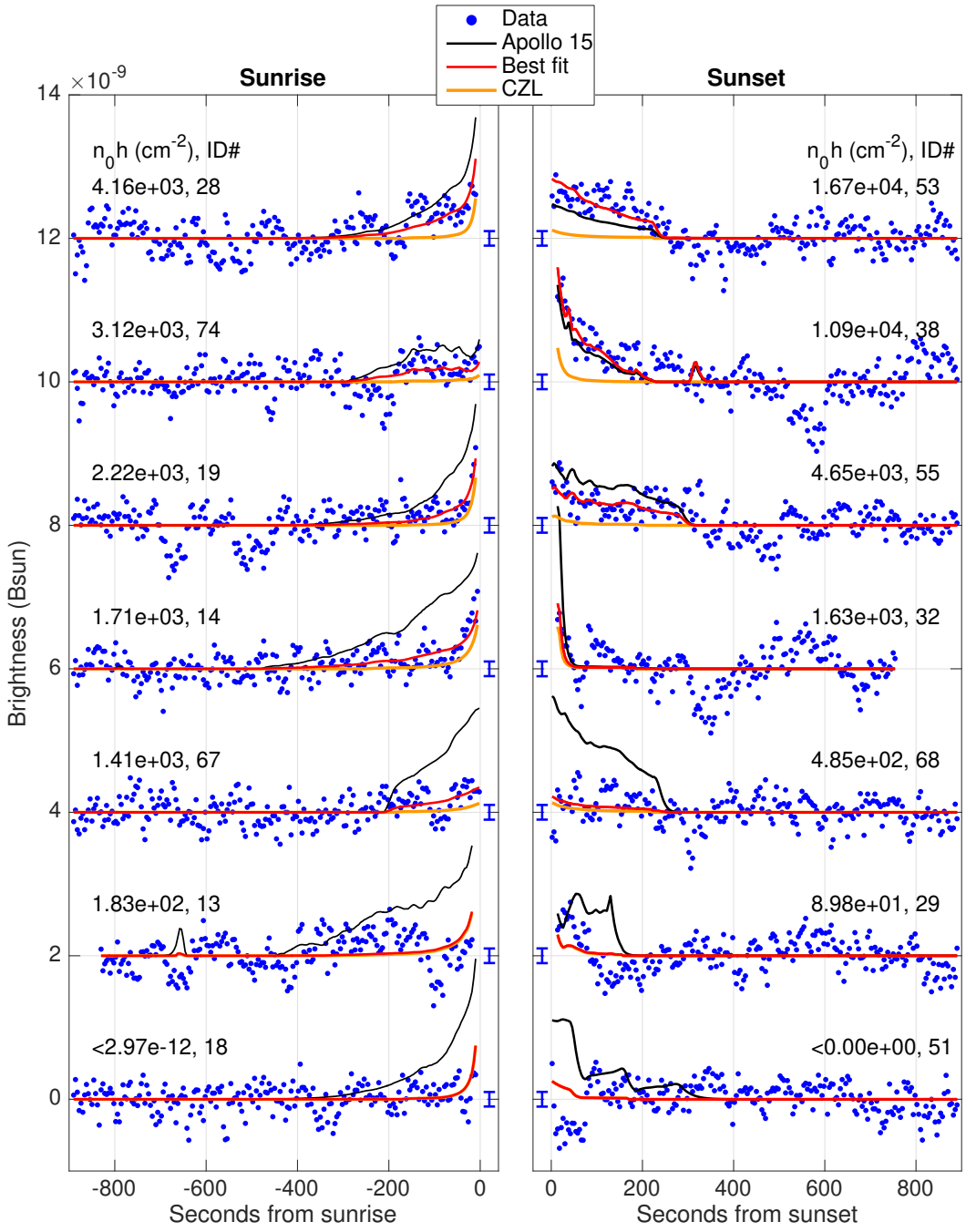

Figure 14. Dark-subtracted data (blue points) for a subset of off-stream scans offset vertically from zero in order of increasing n_0h (bottom to top). The best-fit model (red line) is usually smaller than the Apollo 15 fiducial model (black line, $n_0h = 8500$ cm^{-2}). Both models include the CZL component (orange line). The best-fit value of n_0h and scan ID# are listed for each scan. Each data point is a 4-sec average of 112 full-rate measurements. Error bars show the typical standard error of these averages for each scan.

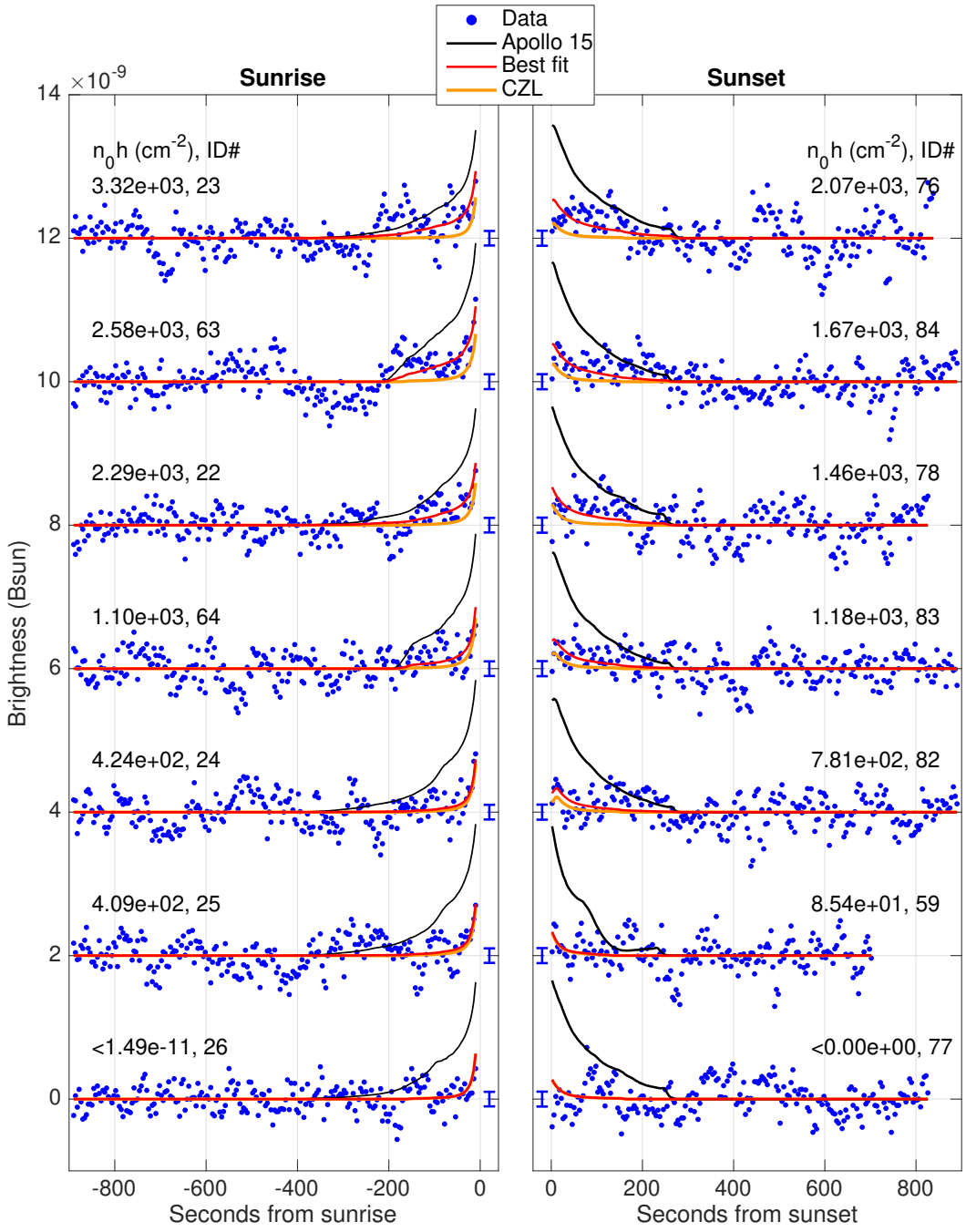

Figure 15. Same as Figure 14 but for the on-stream sample.

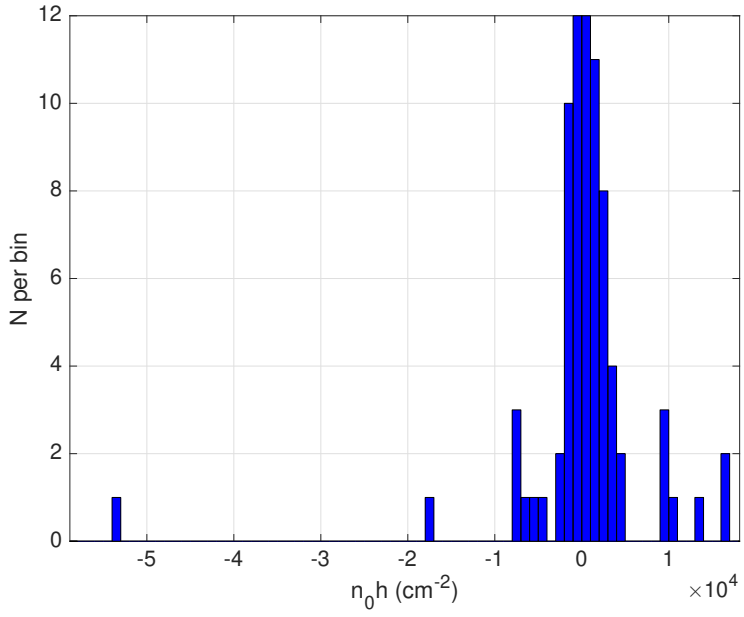

Figure 16. Distribution of best-fit n_0h values with no positivity constraint.

axis) results in a roughly symmetric distribution of n_0h (Figure 16) and the remaining 40% having negative values with a median absolute value of 1321 cm^{-2}. While clearly unphysical, these cases demonstrate the substantial contribution of dark noise to the spread in n_0h values. We note that, although the unconstrained fits are important to understand the dispersion in retrieved dust densities, only positive-constrained retrievals are used for deriving dust limits.

There are 7 scans with values larger than the Apollo 15 measurement, yet the negative tail of the unconstrained distribution implies that some or all of these may be due to dark noise. Figure 17 shows examples of scans with extreme positive and negative n_0h values. Some of these scans have relatively weak fiducial Apollo 15 signals (black lines) perhaps due to unfavorable geometry which limits their ability to constrain a lunar dust signal. The 13 scans with a maximum fiducial Apollo 15 signal $< 6{\times}10^{-10}$ B_{sun} (corresponding to a signal-to-noise ratio of ~ 2) have a median absolute $n_0h \sim 5$ times larger than the rest of the sample. Since we co-estimate the dark current and lunar dust signal, it is possible that in these unfavorable cases, the fit is overly sensitive to dark noise, which can exhibit correlated variations lasting for ~ 200 sec. Excluding these scans leaves 3 with n_0h values greater than Apollo 15. If we force the fitting procedure to use the null-

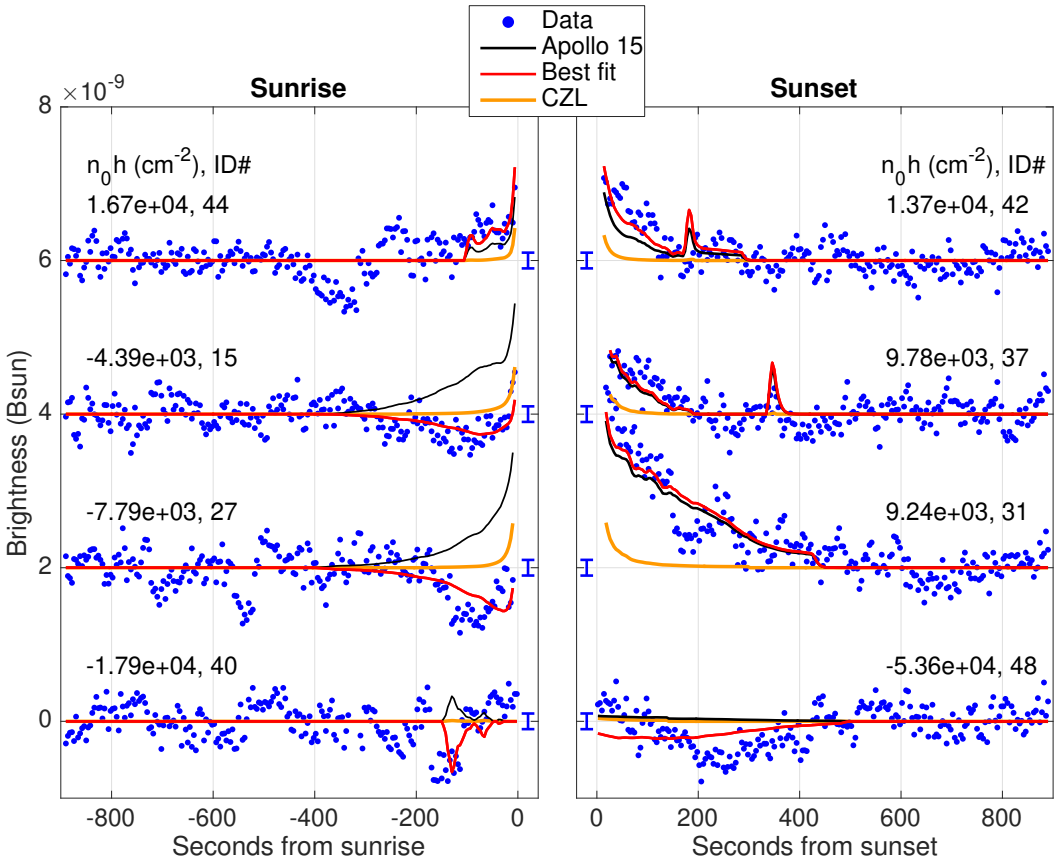

Figure 17. Same as Figure 14 but for examples of scans with extreme n_0h values and no positivity constraint.

hypothesis dark current models, then n_0h typically decreases by a factor of $\sim$ 2 leaving only one value larger than Apollo 15.

Another possible contributor to the n_0h values is the temporally variable solar K-corona that was filtered out in the master composite CZL image. The individual LASCO images in 2016 are generally brighter than the master composite with localized enhancements in excess of 10^{-9} B_{sun} within elongation angles of $\sim 1°$. Re-fitting the data after excluding all points with any boresights within 1° of the Sun typically changes the n_0h values by only a few hundred cm^{-2} and leaves their overall distribution unchanged, which suggests that the time-variable K-corona is not a significant contributor to n_0h. This is consistent with the lack of a clear trend with time in the n_0h values as might be expected due to the declining solar activity in 2016−2017. If we use the LASCO composite image from 2016 DOY 014 to build the CZL model for each scan, the majority

of n_0h values decrease by $\sim 0-500$ cm^{-2}. In another test, we superimposed a bright K-corona streamer on top of the CZL model for every scan using the upper envelope of curves in Figure 7 multiplied by each scan's visibility. This test indicated that bright streamers would be unlikely to shift the density distribution as a whole by more than ~ 300 cm^{-2}, or $\sim 40\%$ of the on-stream median density.

In Figure 18, we show the effect of grain radius on the best-fit n_0h values. We assume that n_0h scales proportionally with the average grain brightness calculated for the different radii using the method in Section 4. The dust density depends strongly on grain radius, decreasing by nearly 4 orders of magnitude from a radius of 0.05 μm to 0.3 μm. This is due to the strong dependence of the grain cross section and scattering efficiency on radius. A less sensitive quantity is the overlying column mass density, for which the dashed gray curves show lines of constant value assuming a grain density of 3 g cm^{-3}. The overlying column mass density decreases by less than 2 orders of magnitude over the same radius range.

The bulk of the on-stream sample has overlying column mass density $\sim 10^{-11}$ g cm^{-2} for $r = 0.1\ \mu m$. This is $\sim 10-100$ times greater than the upper limits from LRO-LAMP spectra (Feldman et al., 2014) and Clementine ST images (Glenar et al., 2014). However, these studies did not observe the exosphere during major meteor stream periods and were, thus, unable to test the role of streams in generating Apollo 15-like LHG. While we do not have the sensitivity of these studies, our on-stream measurements are still able to place useful limits during stream periods which are a factor of ~ 10 lower than the Apollo 15 estimate.

6 Summary and Conclusions

Apollo 15 coronal photography showed evidence for LHG at the dawn terminator at altitudes of $1-30$ km and elongation angles of $1-6^\circ$ (McCoy, 1976; Glenar et al., 2011). These observations have been hypothesized to be due to meteor stream impact ejecta initiating a saltation-like cascade of ejecta with dust grain radius $r \sim 0.1$ μm (Glenar et al., 2011). Recent results from LRO-LAMP and Clementine STs placed limits on the concentration of similarly sized grains $\sim 100-1000$ times less than Apollo 15 at altitudes of $\sim 1-20$ km during periods outside of major meteor streams (Feldman et al., 2014; Glenar et al., 2014, respectively). LADEE-LDEX also found no evidence for the

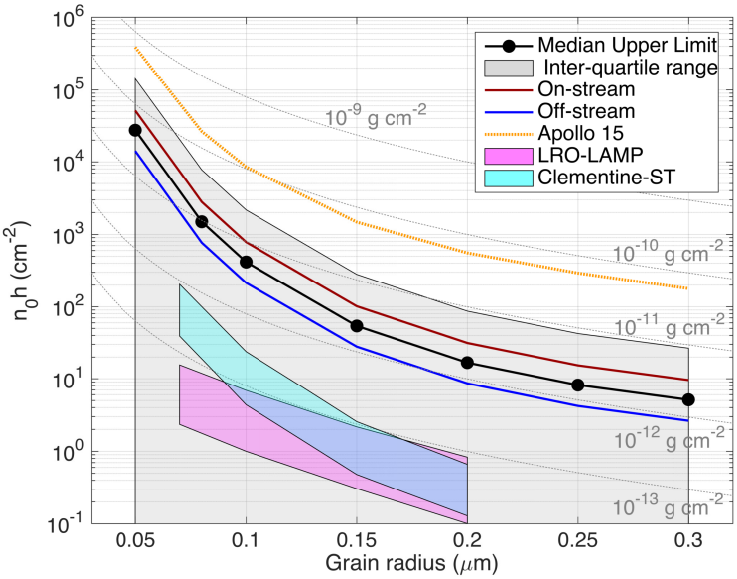

Figure 18. Upper limit on the vertical column density, $n_0 h$ as a function of dust grain radius. The median (black line and points) and inter-quartile range (gray shaded region) of the whole sample are compared to the median of the on-stream (brown) and off-stream (blue) sub-samples. The pink and cyan shaded regions show the range of densities from LRO-LAMP (Feldman et al., 2014) and Clementine-ST (Glenar et al., 2014) observations. Dashed gray curves with labels denote lines of constant vertical column mass density assuming a grain density of 3 g cm^{-3}.

putative dust population, and placed similar limits on the dust concentration, but did not reach altitudes $\lesssim$ 30 km during major meteor streams (Szalay & Horányi, 2015).

Motivated by the relative lack of constraints on the role of meteor streams in producing LHG at the same altitudes and elongation angles observed by Apollo 15, we conducted a 2-year-long campaign to monitor the lunar dust exosphere for enhancements in the concentration of $\sim$ 0.1 μm-size dust grains at altitudes $<$ 20 km both during and outside of major meteor stream periods. The LOLA-LR telescope on LRO is capable of probing arbitrarily small elongation angles at any time of year, in contrast to the LRO nadir-pointing instruments, allowing us to test the hypothesis that major meteor streams can produce LHG similar to what was measured by Apollo 15.

In this work, we find that the on-stream and off-stream samples are statistically indistinguishable, and that the Apollo 15 dust density is greater than all of the densities inferred for the on-stream sample. Together with the results of previous studies de-

scribed above, our results show that it is highly likely that this phenomenon is a rare occurrence at altitudes < 20 km during major meteor streams. We cannot completely rule out a lower-level LHG pervasive during stream periods, but our results place an upper limit of $\sim 10^{-11}$ g cm^{-2} for the overlying column mass density assuming a grain radius of ~ 0.1 μm and grain density of 3 g cm^{-3}. This limit is roughly 10 times lower than the Apollo 15 measurement.

This study is the first to quantitatively constrain the role of meteoroid streams in producing Apollo 15-like LHG at altitudes < 20 km and small elongation angles, and further narrows the properties of this high-altitude LHG and the conditions under which it can occur. Any LHG occurring entirely within ~ 1 km of the surface is unconstrained by these measurements due to the high-altitude observing geometry and large FOV of the LR telescope.

Acknowledgments

Data and derived data products used here, including LOLA data, LASCO images, and modeling results are available from the LOLA PDS Data Node (`http://imbrium.mit.edu`) and the Planetary Geodynamics Data Archive (`https://pgda.gsfc.nasa.gov`). LASCO data may also be downloaded from the Naval Research Laboratory LASCO website (`https://lasco-www.nrl.navy.mil`). The SOHO/LASCO data used here are produced by a consortium of the Naval Research Laboratory (USA), Max-Planck-Institut fuer Aeronomie (Germany), Laboratoire d'Astronomie (France), and the University of Birmingham (UK). SOHO is a project of international cooperation between ESA and NASA. We are grateful to the LRO Mission Operations Team for planning and executing the spacecraft slews, Althea Moorhead at the NASA Meteoroid Environment Office for providing meteor shower predictions, and Tim Stubbs and Dave Glenar for useful discussions regarding lunar dust, CZL, and illumination modeling.

References

Barker, M. K., Sun, X., Mazarico, E., Neumann, G. A., Zuber, M. T., & Smith, D. E. (2016, July). Lunar phase function at 1064 nm from Lunar Orbiter Laser Altimeter passive and active radiometry. Icarus, *273*, 96-113. doi: 10.1016/j.icarus.2016.02.008

Bean, e. a., A. L. (1970). Apollo 12: Preliminary Science Report. NASA SP-235. *NASA Special Publication*, *235*.

Colaprete, A., Sarantos, M., Wooden, D. H., Stubbs, T. J., Cook, A. M., & Shirley, M. (2016, Jan). How surface composition and meteoroid impacts mediate

sodium and potassium in the lunar exosphere. *Science*, *351*(6270), 249-252. doi: 10.1126/science.aad2380

Colwell, J. E., Batiste, S., Horányi, M., Robertson, S., & Sture, S. (2007, June). Lunar surface: Dust dynamics and regolith mechanics. *Reviews of Geophysics*, *45*, RG2006. doi: 10.1029/2005RG000184

Costello, E. S., Ghent, R. R., & Lucey, P. G. (2018, November). The mixing of lunar regolith: Vital updates to a canonical model. Icarus, *314*, 327-344. doi: 10.1016/j.icarus.2018.05.023

Criswell, D. R. (1972). Lunar dust motion. In A. E. Metzger, J. I. Trombka, L. E. Peterson, R. C. Reedy, & J. R. Arnold (Eds.), *Lunar and planetary science conference proceedings* (Vol. 3, p. 2671).

Egan, W. G., & Hilgeman, T. (1973, October). Optical constants for terrestrial analogs of lunar materials. AJ, *78*, 799. doi: 10.1086/111486

Feldman, P. D., Glenar, D. A., Stubbs, T. J., Retherford, K. D., Randall Gladstone, G., Miles, P. F., ... Alan Stern, S. (2014, May). Upper limits for a lunar dust exosphere from far-ultraviolet spectroscopy by LRO/LAMP. Icarus, *233*, 106-113. doi: 10.1016/j.icarus.2014.01.039

Giese, R. H., Kneissel, B., & Rittich, U. (1986, December). Three-dimensional models of the zodiacal dust cloud - A comparative study. Icarus, *68*, 395-411. doi: 10.1016/0019-1035(86)90046-1

Glenar, D. A., Stubbs, T. J., Hahn, J. M., & Wang, Y. (2014, December). Search for a high-altitude lunar dust exosphere using Clementine navigational star tracker measurements. *Journal of Geophysical Research (Planets)*, *119*, 2548-2567. doi: 10.1002/2014JE004702

Glenar, D. A., Stubbs, T. J., McCoy, J. E., & Vondrak, R. R. (2011, November). A reanalysis of the Apollo light scattering observations, and implications for lunar exospheric dust. Planet. Space Sci., *59*, 1695-1707. doi: 10.1016/j.pss.2010.12.003

Glenar, D. A., Stubbs, T. J., Schwieterman, E. W., Robinson, T. D., & Livengood, T. A. (2019, March). Earthshine as an illumination source at the Moon. Icarus, *321*, 841-856. doi: 10.1016/j.icarus.2018.12.025

Godwin, R. (2002). *Apollo 17 : the NASA mission reports*.

Grava, C., Stubbs, T. J., Glenar, D. A., Retherford, K. D., & Kaufmann, D. E. (2017, May). Absence of a detectable lunar nanodust exosphere during a search with LRO's LAMP UV imaging spectrograph. Geophys. Res. Lett., *44*, 4591-4598. doi: 10.1002/2017GL072797

Hahn, J. M., Zook, H. A., Cooper, B., & Sunkara, B. (2002, August). Clementine Observations of the Zodiacal Light and the Dust Content of the Inner Solar System. Icarus, *158*, 360-378. doi: 10.1006/icar.2002.6881

Hayes, A. P., Vourlidas, A., & Howard, R. A. (2001, February). Deriving the Electron Density of the Solar Corona from the Inversion of Total Brightness Measurements. ApJ, *548*, 1081-1086. doi: 10.1086/319029

Horányi, M., Szalay, J. R., Kempf, S., Schmidt, J., Grün, E., Srama, R., & Sternovsky, Z. (2015, June). A permanent, asymmetric dust cloud around the Moon. Nature, *522*, 324-326. doi: 10.1038/nature14479

Jenniskens, P. (1994, July). Meteor stream activity I. The annual streams. A&A, *287*, 990-1013.

Katzan, C. M., & Edwards, J. L. (1991, November). *Lunar dust transport and potential interactions with power system components* (Tech. Rep.).

Kim, Y. K., Lee, S. M., Yang, J. H., Kim, J. H., & Kim, C. K. (1971). Mineralogical and chemical studies of lunar fines 10084,148 and 12070,98. In *Lunar and planetary science conference proceedings* (Vol. 2, p. 747).

King, E. A., Jr., Butler, J. C., & Carman, M. F., Jr. (1971). The lunar regolith as sampled by Apollo 11 and Apollo 12: Grain size analyses, modal analyses, and origins of particles. In *Lunar and planetary science conference proceedings*

(Vol. 2, p. 737).

Leinert, C., Bowyer, S., Haikala, L. K., Hanner, M. S., Hauser, M. G., Levasseur-Regourd, A.-C., ... Witt, A. N. (1998, January). The 1997 reference of diffuse night sky brightness. A&AS, *127*, 1-99. doi: 10.1051/aas:1998105

Mao, D., McGarry, J. F., Mazarico, E., Neumann, G. A., Sun, X., Torrence, M. H., ... Zuber, M. T. (2017, February). The laser ranging experiment of the Lunar Reconnaissance Orbiter: Five years of operations and data analysis. Icarus, *283*, 55-69. doi: 10.1016/j.icarus.2016.07.003

Mazarico, E., Barker, M. K., & Nicholas, J. B. (2018, Dec). Advanced illumination modeling for data analysis and calibration. Application to the Moon. *Advances in Space Research*, *62*(11), 3214-3228. doi: 10.1016/j.asr.2018.08.022

Mazarico, E., Neumann, G. A., Smith, D. E., Zuber, M. T., & Torrence, M. H. (2011, February). Illumination conditions of the lunar polar regions using LOLA topography. Icarus, *211*, 1066-1081. doi: 10.1016/j.icarus.2010.10.030

McCoy, J. E. (1976, April). Photometric studies of light scattering above the lunar terminator from Apollo solar corona photography. In D. C. Kinsler (Ed.), *Lunar and planetary science conference proceedings* (Vol. 7, p. 1087-1112).

McCoy, J. E., & Criswell, D. R. (1974). Evidence for a high altitude distribution of lunar dust. In *Lunar and planetary science conference proceedings* (Vol. 5, p. 2991-3005).

Molau, S., Barentsen, G., & Nikolic, V. (2018). *MeteorFlux.org.* `https://meteorflux.org`.

Morrill, J. S., Korendyke, C. M., Brueckner, G. E., Giovane, F., Howard, R. A., Koomen, M., ... Andrews, M. (2006, February). Calibration of the Soho/Lasco C3 White Light Coronagraph. Sol. Phys., *233*, 331-372. doi: 10.1007/s11207-006-2058-1

Rennilson, J. J., & Criswell, D. R. (1974, June). Surveyor Observations of Lunar Horizon-Glow. *Moon*, *10*, 121-142. doi: 10.1007/BF00655715

Sato, H., Robinson, M. S., Hapke, B., Denevi, B. W., & Boyd, A. K. (2014, August). Resolved Hapke parameter maps of the Moon. J. Geophys. Res.*: Planets*, *119*, 1775-1805. doi: 10.1002/2013JE004580

Severnyi, A. B., Terez, E. I., & Zvereva, A. M. (1975, September). The measurements of sky brightness on Lunokhod-2. *Moon*, *14*, 123-128. doi: 10.1007/BF00562978

Shkuratov, Y., Starukhina, L., Hoffmann, H., & Arnold, G. (1999, February). A Model of Spectral Albedo of Particulate Surfaces: Implications for Optical Properties of the Moon. Icarus, *137*, 235-246. doi: 10.1006/icar.1998.6035

Smith, D. E., Zuber, M. T., Jackson, G. B., Cavanaugh, J. F., Neumann, G. A., Riris, H., ... Zagwodzki, T. W. (2010, January). The Lunar Orbiter Laser Altimeter investigation on the Lunar Reconnaissance Orbiter mission. *Space Sci. Rev.*, *150*, 209-241. doi: 10.1007/s11214-009-9512-y

Smith, D. E., Zuber, M. T., Neumann, G. A., Mazarico, E., Lemoine, F. G., Head, J. W., III, ... Mcclanahan, T. (2017, February). Summary of the results from the lunar orbiter laser altimeter after seven years in lunar orbit. Icarus, *283*, 70-91. doi: 10.1016/j.icarus.2016.06.006

Speyerer, E. J., Povilaitis, R. Z., Robinson, M. S., Thomas, P. C., & Wagner, R. V. (2016, October). Quantifying crater production and regolith overturn on the Moon with temporal imaging. Nature, *538*, 215-218. doi: 10.1038/nature19829

Stephens, G. L., O'Brien, D., Webster, P. J., Pilewski, P., Kato, S., & Li, J.-l. (2015, March). The albedo of Earth. *Reviews of Geophysics*, *53*, 141-163. doi: 10.1002/2014RG000449

Stubbs, T. J., Glenar, D. A., Colaprete, A., & Richard, D. T. (2010, Apr). Optical scattering processes observed at the Moon: Predictions for the LADEE Ultraviolet Spectrometer. *Planetary and Space Science*, *58*(5), 830-837. doi:

10.1016/j.pss.2010.01.002

Stubbs, T. J., Vondrak, R. R., & Farrell, W. M. (2006). A dynamic fountain model for lunar dust. *Advances in Space Research*, *37*, 59-66. doi: 10.1016/j.asr.2005.04.048

Szalay, J. R., & Horányi, M. (2015, July). The search for electrostatically lofted grains above the Moon with the Lunar Dust Experiment. Geophys. Res. Lett., *42*, 5141-5146. doi: 10.1002/2015GL064324

Szalay, J. R., & Horányi, M. (2016, May). Lunar meteoritic gardening rate derived from in situ LADEE/LDEX measurements. Geophys. Res. Lett., *43*, 4893-4898. doi: 10.1002/2016GL069148

Szalay, J. R., Poppe, A. R., Agarwal, J., Britt, D., Belskaya, I., Horányi, M., ... Spahn, F. (2018, August). Dust Phenomena Relating to Airless Bodies. Space Sci. Rev., *214*, 98. doi: 10.1007/s11214-018-0527-0

van de Hulst, H. C. (1957). *Light Scattering by Small Particles*.

Wang, X., Schwan, J., Hsu, H.-W., Grün, E., & Horányi, M. (2016, June). Dust charging and transport on airless planetary bodies. Geophys. Res. Lett., *43*, 6103-6110. doi: 10.1002/2016GL069491

Wooden, D. H., Cook, A. M., Colaprete, A., Glenar, D. A., Stubbs, T. J., & Shirley, M. (2016, September). Evidence for a dynamic nanodust cloud enveloping the Moon. *Nature Geoscience*, *9*, 665-668. doi: 10.1038/ngeo2779

Zook, H. A., & McCoy, J. E. (1991, November). Large scale lunar horizon glow and a high altitude lunar dust exosphere. Geophys. Res. Lett., *18*, 2117-2120. doi: 10.1029/91GL02235

Zuber, M. T., Smith, D. E., Zellar, R. S., Neumann, G. A., Sun, X., Katz, R. B., ... Zagwodzki, T. W. (2010, January). The Lunar Reconnaissance Orbiter laser ranging investigation. Space Sci. Rev., *150*, 63-80. doi: 10.1007/s11214-009-9511-z

Supporting Information for "Searching for lunar horizon glow with the Lunar Orbiter Laser Altimeter"

M. K. Barker[1], E. Mazarico[1], T. P. McClanahan[1], X. Sun[1], G. A. Neumann[1],

D. E. Smith[2], M. T. Zuber[2], J. W. Head[3]

[1]Goddard Space Flight Center, 8800 Greenbelt Rd., Greenbelt, MD 20771

[2]Dept. of Earth, Atmospheric and Planetary Sciences, MIT, 77 Massachusetts Ave. Cambridge, MA 02139

[3]Dept. of Earth, Environmental and Planetary Sciences, Brown Univ., Providence, RI 02912

Contents of this file

1. Figures S1 to S3

Additional Supporting Information (Files uploaded separately)

1. Table S1

Introduction

The supporting information contains Figures S1 to S3 and Table S1.

Corresponding author: M. K. Barker, Goddard Space Flight Center, 8800 Greenbelt Rd., Greenbelt, MD 20771, USA. (michael.k.barker@nasa.gov)

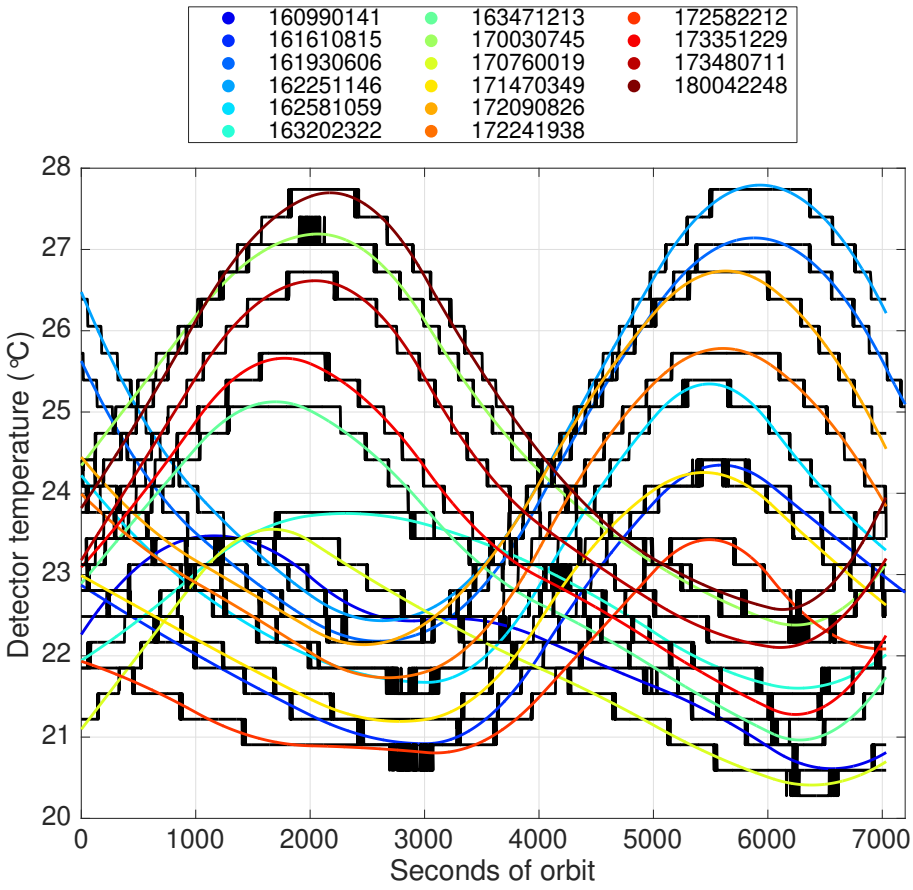

Figure S1: Detector 1 temperature as a function of time in orbit. The black lines are the temperature readings from the LOLA housekeeping telemetry. The colored lines are piecewise cubic spline fits. Only a few scans are shown out of the whole sample for clarity.

To convert the model 1064-nm earthshine into counts/sec we obtained a preliminary near-IR radiance calibration for Channel 1. We chose 3 orbits from 2016 to 2017 (LOLA Reduced Data Records 162191111, 170260837, and 172071130) with low beta angles to sample a wide dynamic range. We compared the daytime noise counts measured in Channel 1 for the lunar far side surface to the actual radiance measured by the other channels in the same shots (Figure S2) adopting the near-IR calibration of Channels 2-5 from Barker et al. (2016). We do not model the Channel 1 temperature dependence as this will have a secondary impact on the results relative to

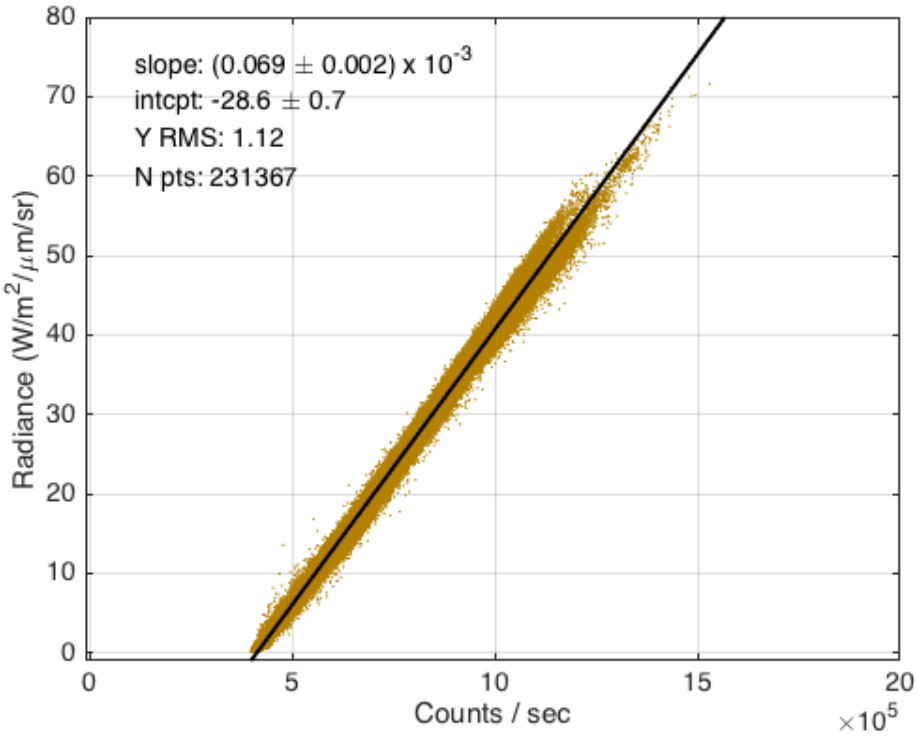

Figure S2: Channel 1 radiance calibration for the LOLA receiver telescope at 1064-nm. The x-axis shows the average counts/sec in channel 1 and the y-axis shows the 1064-nm radiance using the calibration of Barker et al. (2016) on the average counts/sec in channels $2-5$.

other approximations we have made, such as the Earth reflectance law and albedo. The best-fit slope is then used to convert the model 1064-nm earthshine into counts/sec, which is then added to the counts/sec from the LR telescope at 532-nm. The sum of both count rates is scaled into an effective 532-nm radiance using the same calibration factor as for the data. The zero-point in Fig. S2 reflects the mean dark current level during these time periods. Figure S2 also shows that the detector response is linear up to at least half the saturation level.

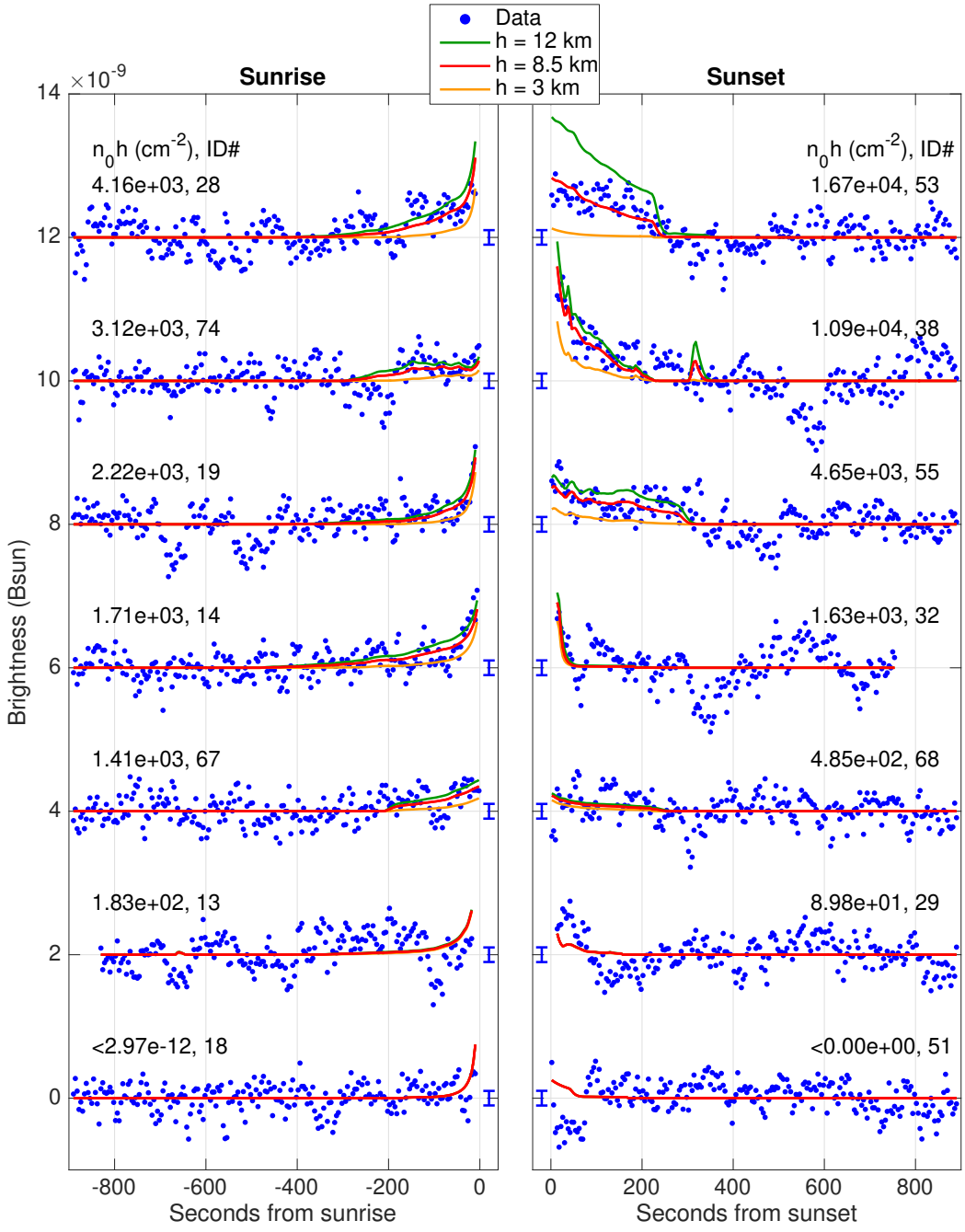

Figure S3: Same as Figure 14, but showing the effect of varying the scale height of the best-fit model (red line, $h = 8.5$ km) to 3 km (orange line) or 12 km (green line) while holding n_0 fixed.

Table S1: Summary of all executed limb scans.

Column 1: Scan ID#.

Column 2: Universal Coordinated Time of last measured point just before sunrise or after sunset.

Column 3: Day-of-year (DOY).

Column 4: Beta angle in degrees.

Column 5: Longitude (degrees) of central boresight tangent point at sunrise or sunset.

Column 6: Latitude (degrees) of central boresight tangent point at sunrise or sunset.

Column 7: Local solar time ($0 - 24$ hours).

Column 8: Notes. Sunrise (SR) or sunset (SS). SS+SR indicates a grazing double-scan from sunset to sunrise. Meteor shower designation if applicable: Geminids (GEM), Leonids (LEO), Perseids (PER), Quadrantids (QUA), Southern Delta Aquariids (SDA).

Column 9: On- or off-stream sample designation. Not applicable (N/A) for stream scans on the opposite hemisphere as the stream radiant. See text for details.

Column 10: Best-fit vertical column dust density $n_0 h$ (cm^{-2}). N/A for scans that were discarded.

Column 11: LOLA RDR containing the scan (format: YYDOYHHMM).

References

Barker, M. K., Sun, X., Mazarico, E., Neumann, G. A., Zuber, M. T., & Smith, D. E. (2016, July). Lunar phase function at 1064 nm from Lunar Orbiter Laser Altimeter passive and active radiometry. Icarus, *273*, 96-113. doi: 10.1016/j.icarus.2016.02.008